


## Experimental and numerical investigations on rotor noise in axial descending flight

Yuhong Li , Xiangtian Li , Han Wu , Peng Zhou , and Xin Zhang\*

*Department of Mechanical and Aerospace Engineering, The Hong Kong University of Science and Technology, Clear Water Bay, Kowloon, Hong Kong Special Administrative Region of China*

Siyang Zhong †

*Department of Aeronautical and Aviation Engineering, The Hong Kong Polytechnic University, Hung Hom, Kowloon, Hong Kong Special Administrative Region of China*



(Received 18 May 2023; accepted 18 August 2023; published 28 September 2023)

While various aerodynamic noise generation mechanisms and characteristics have been extensively studied for drone research, the noise features during the descending flight state have not been well addressed. In this work, we investigate the aerodynamics and aeroacoustics of a two-bladed drone rotor operating in descent using both experimental and numerical approaches. First, we measure the rotor thrust and torque in an anechoic wind tunnel at various rotational speeds and descent rates. The results reveal a significant loss of mean thrust and strong thrust fluctuations with the increase of descent rates due to the formation of highly unsteady vortex rings. The measured acoustic spectra show multiple humps occurring at the blade passing frequency and its harmonics. Next, we perform numerical simulations based on the delayed detached eddy simulations to gain more understanding of the noise generation mechanisms. The computed integrated aerodynamic forces and acoustic spectra agree well with the experimental results. We present nearfield flow structures that demonstrate the gradual formation process of the vortex ring and the complex turbulent wake structures. Notably, the computed aeroacoustic characteristics exhibit a similar tendency with respect to the descent rate to the experimental results. Moreover, the simulation results suggest that the additional noise has a radiation directivity in the axial direction perpendicular to the rotation plane. Finally, we conduct a noise source analysis on the blade surface based on the simulation results, revealing that the strong leading-edge sources are likely related to the blade-wake interaction process during descending flight.

DOI: [10.1103/PhysRevFluids.8.094803](https://doi.org/10.1103/PhysRevFluids.8.094803)

### I. INTRODUCTION

Since the early 2010s we have witnessed a fast development of small unmanned aerial vehicles [1]. The success encourages the development of larger multirotor vehicles for future urban air mobility [2,3]. Due to the use of clean energy such as electricity for propulsion and the operation at low altitudes, the inevitable noise pollution is likely to be a critical limiting factor of public acceptance [4]. Among various noise sources, rotor noise is the dominant aerodynamic noise source for a multirotor vehicle, which is favored among various aircraft configurations due to its easy maneuverability and vertical take-off and landing capability. Therefore, extensive and continuous

---

\*aexzhang@ust.hk

†siyang.zhong@polyu.edu.hk

efforts on drone rotors have been made to understand the noise mechanisms [5–9] and promote low-noise designs [10,11] in the past few years.

The rotor noise contains tonal and broadband contents, with distinctly different acoustic characteristics [12]. The tonal noise is usually associated with the rotor’s periodical rotation, showing spectral peaks at the rotor’s blade passing frequency (BPF) and its harmonics. Typical tonal noise sources include thickness noise and steady loading noise, which have been well studied and understood by analytical studies [13–15]. In practical rotor operations, unsteady sources such as blade-vortex interaction [16], rotor-support interaction [17], rotational speed variation [5,18], and blade vibration [19] may produce unsteady loadings acting on blade surfaces, leading to additional tonal noise at higher harmonics of BPF. In contrast, broadband noise consists of random unsteadiness in a wide frequency range and generally comes from the interaction between turbulence and the blade surface. Although tremendous efforts have been made to build the broadband noise prediction model for rotors [20–22], accurate rotor noise prediction is still challenging for low-fidelity methods. As a result, considerable experimental efforts have been made to quantify and characterize the rotor noise. Yang *et al.* [23] experimentally conducted parametric studies on an isolated rotor in forward flight and proposed noise prediction models by polynomial fittings. Gojon *et al.* [9] performed measurements for different isolated small-scale rotors in hovering conditions to provide an open database for numerical simulations. The turbulence ingestion effect on rotor noise was investigated by Yauwenas *et al.* [24] by placing the rotor downstream of a turbulence mesh grid. The results show additional acoustic excitations at high-order BPF harmonics. Considering the airfoil profile deviations due to practical manufacturing error, Wu *et al.* [25] experimentally investigated the rotor noise of three modified airfoil profiles with different trailing-edge thicknesses. They observed that the finite trailing edge thickness could lead to a discernible noise reduction under strong axial flows. Some researchers prefer high-fidelity numerical simulations due to their high controllability and low uncertainty. Casalino *et al.* [26] numerically simulated the noise of a small drone rotor operating at different advance ratios based on a lattice-Boltzmann method and Ffowcs-Williams and Hawkings (FW-H) integral solution. They compared the simulated results with experimental measurements and identified the transition flow regime on the blade suction side. Romani *et al.* [7] numerically studied the effect of the inflow with different angles and found that an angular inflow could lead to periodic unsteady loadings and noise directivity change. Similarly, Nardari *et al.* [27] also conducted the lattice-Boltzmann simulations to investigate the recirculation effect inside a closed anechoic chamber. They found that extra BPF tones at high BPF harmonics were observed for confined simulations compared to the unconfined ones, which was attributed to the recirculated turbulence ingesting effect. There are also research efforts considering the interactional effect of different aircraft components on noise generation, such as the rotor-rotor interaction [28], rotor-support interaction [17,29] and rotor-wing interaction [6]. The main impacts of these interactions of different types are the additional tonal impulses at harmonics of BPF and modified directivities caused by the induced unsteady loadings.

As described above, despite the fact that various noise generation mechanisms for small-scale rotors have been investigated, most studies have focused primarily on hover and forward flight conditions. In contrast, the descending flight mode is rarely addressed. Although the descent stage constitutes only a part of the whole flight mission, it is usually considered the most dangerous flight stage due to the highly unsteady flow physics [30]. According to the existing study of helicopter aerodynamics [31], the descending flight generally consists of four different states, namely the normal working state, the vortex ring state (VRS), the turbulent wake state and the windmill brake state, with the increase of descent rate. The VRS is considered a critical flow condition and receives the most attention. A sizable toroidal vortex structure accumulates around the rotor blade tips under the VRS, leading to significant interactions with rotor blades. As an extensively investigated phenomenon for helicopters, the VRS results in a thrust loss [32] and strong thrust oscillations [30] such that more shaft torque is required [33]. However, relevant studies for small-scale drone rotors are still insufficient, and it is unclear if the results based on helicopters are applicable to drone rotors

with much lower Reynolds and Mach numbers. Shetty and Selig [34] performed an experiment campaign on small-scale rotors with different geometries in axial descending flight. They suggest that the thrust reduction and the fluctuation are both highly dependent on the blade pitch. Kinzel *et al.* [35] numerically examined the aerodynamic performance of a coaxial rotor in descent, showing that the coaxial configuration has less thrust loss than an isolated rotor. Throneberry *et al.* [36] experimentally performed flow visualization for a complete drone model to investigate the wake characteristics in various flight conditions. Their results indicate that there is a transition when the rotor wake below the vehicle propagates to above the vehicle as the descent ratio increases. More recently, the twin-rotor configuration and the corresponding interactional effect between two rotors were considered by Chae *et al.* [37] and Veismann *et al.* [38], respectively. Chae *et al.*'s results reveal that the wake between the rotors is highly dependent on the tip distance between rotors, whereas the outer region is rarely affected. In contrast, Veismann *et al.*'s work focused more on the aerodynamic performance, suggesting that the mean thrust of a dual-rotor system can be described by a single-rotor setup when the tip distance is larger than 1.5 times the rotor diameter. Veismann *et al.* also [39] systematically assessed the descent performance of rotors of different geometries by wind tunnel measurements, showing that rotors with a larger aspect ratio and blade loading coefficient can lead to superior aerodynamic performance and are able to suppress the VRS-induced vibrations. Despite the adverse aerodynamic effect of the VRS on rotor performance is already studied by numerous researchers, the corresponding acoustic response, to the authors' knowledge, is hardly considered in previous studies. To date, the descent rate of a commercial drone is restricted to a relatively low value to avoid the occurrence of VRS. However, future rotor designs and advanced control systems may enable a more aggressive descent rate to allow for agile operations and flexible trajectories. The descending flight becomes even more important for urban air mobility vehicles that are anticipated to take off and land routinely in populated urban areas. Therefore, understanding the aeroacoustic characteristics of rotors in axial descending flight is essential for low-noise designs and optimal flight trajectory planning.

In this work, we investigate the aerodynamic performance and the corresponding acoustic feature of a well-designed small-scale rotor in axial descent. First, we conduct experiments in an anechoic wind tunnel and measure the thrust, torque, and acoustic data by a high-accuracy load cell and a curved microphone array at different rotational and descent rates. Then, we use high-fidelity CAA simulations based on delayed detached eddy simulations (DDES) [40] to provide insight into flow structures and help identify the sound generation mechanisms. The experiments validate the results of the numerical simulations, and the discrepancies are also discussed.

The remainder of this paper is organized as follows. Sections II and III describe the experimental setup and the numerical methodologies, respectively. Section IV presents the results of the integrated aerodynamic performance, the flow structures and the acoustic characteristics, followed by relevant discussions. Section V summarises this study.

## II. EXPERIMENTAL METHODS

### A. Rotor model

Figure 1(a) shows the geometry of the two-blade rotor named SalonPro 2 (SP2) [11] used in this work, which has a diameter of  $D = 0.218$  m. The rotor blade has a cross section of a NACA4412 airfoil along the span. Figure 1(b) shows the airfoil chord length and pitch angle distribution.

### B. Experimental setup

The experiments were conducted in an anechoic wind tunnel facility with dimensions of 3.3 m (length)  $\times$  3.1 m (width)  $\times$  2.0 m (height) [41]. Figure 2 shows the schematic and the photos of the experimental configuration. The test platform is installed between the open-jet inflow duct and the jet collector. The real-time rotational speed is measured by an optical rotary encoder (100 pulses per revolution) mounted behind a twin-shaft brushless dc motor. A load cell with six degrees of

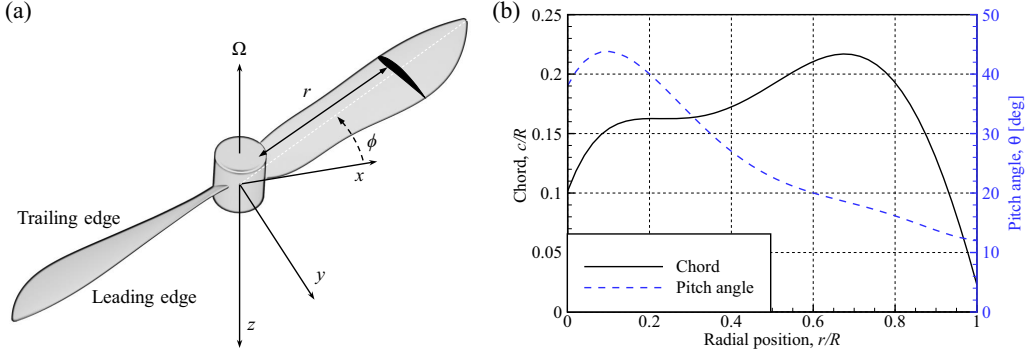


FIG. 1. (a) Rotor geometry and the coordinate system. (b) Rotor chord and pitch distribution.

freedom is used to record the aerodynamic loadings. The motor, the rotational speed controller and the load cell are all embedded in a streamlined fairing to minimize their influence on the wake. The supporting tower is designed to be far away enough from the rotor hub (more than twice the rotor radius) such that the rotor-struct interaction noise is minimized [17,29]. In this work, the struct is placed upstream of the rotor wake to ensure the flow structures in the rotor wake region are not affected by the installation. A detailed discussion on the installation effect of the supporting tower can be found in Appendix A. For acoustic measurements, six 1/2-inch GRAS type 46AE free-field microphones are evenly distributed on a curved array at a distance of 1.5 m ( $6.88D$ ) from the rotor hub. The microphones are labeled from  $M_0$  to  $M_5$  corresponding to the observer angle  $\theta$ , the definition of which is given in Fig. 2, from  $70^\circ$  to  $120^\circ$ . All apparatus and supporting structures were covered with 10-mm-thick polyurethane foam to reduce sound scattering. For each measurement, the data of a duration of 10 s is sampled after the flow is fully developed. The sampling frequencies for the aerodynamic force and noise data are 20 and 50 kHz, respectively. Table I shows an overview of the tested variables. The experiments were conducted under hovering conditions ( $v_d = 0$ ) and at an axial descent rate from  $v_d = 4$  to 10 m/s. The tested rotational speed starts from 60 revolutions per second (RPS) to 120 RPS.

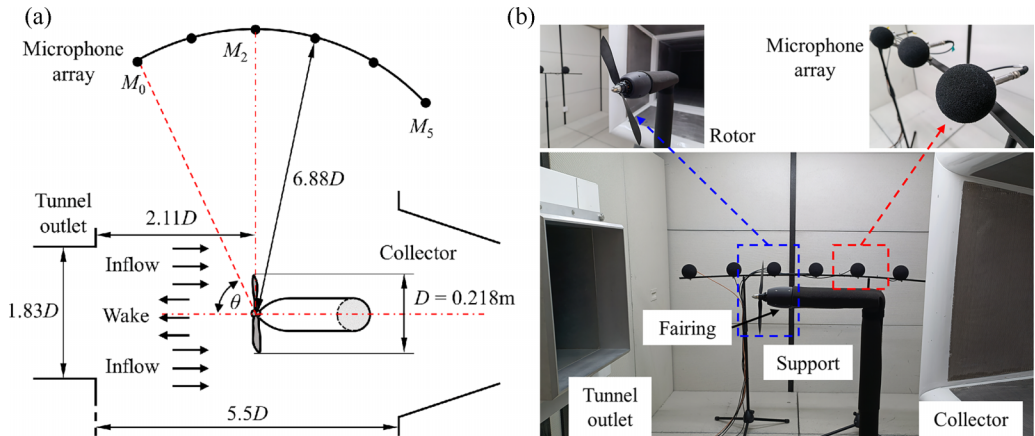


FIG. 2. (a) The schematic and (b) the photos of the experimental setup.

TABLE I. Experimental test matrix.

Testing variable	Descent rate (m/s)	Rotational speed (RPS)
Values	0, 4, 5, 6, 7, 8, 9, 10	60, 70, 80, 90, 100, 110, 120

### III. NUMERICAL METHODS

#### A. Governing equations

The flow is solved based on an acoustic-wave preserved artificial compressibility method [42], which can efficiently capture the acoustic waves in low-Mach-number flows. The governing equations are

$$\begin{aligned} \frac{\partial p}{\partial t} + (\mathbf{u} \cdot \nabla)p + \rho_0 c_0^2 \nabla \cdot \mathbf{u} &= 0, \\ \frac{\partial \mathbf{u}}{\partial t} + (\mathbf{u} \cdot \nabla)\mathbf{u} - \nabla \cdot (\nu \nabla \mathbf{u}) + \frac{1}{\rho_0} \nabla p &= 0, \end{aligned} \quad (1)$$

where  $\rho_0$  and  $c_0$  are the undisturbed flow density and the freestream speed of sound,  $\mathbf{u}$  is the flow velocity,  $\nu$  is the kinematic viscosity, and  $p$  is the static pressure. The DDES is conducted with the one-equation Spalart-Allmaras turbulence model [43] to model the turbulent viscosity  $\tilde{\nu}$  as

$$\frac{\partial \tilde{\nu}}{\partial t} + \mathbf{u} \cdot \nabla \tilde{\nu} = c_{b1} \tilde{S} \tilde{\nu} + \frac{1}{\sigma} \{ \nabla \cdot [(v + \tilde{\nu}) \nabla v] + c_{b2} (\nabla \tilde{\nu})^2 \} - c_{w1} f_w \left( \frac{\tilde{\nu}}{\tilde{d}} \right)^2, \quad (2)$$

where  $\tilde{S}$  is the modified vorticity magnitude;  $f_w$  the function for near-wall damping;  $c_{b1}$ ,  $c_{b2}$ ,  $c_{w1}$ ,  $\sigma$  are all model constants; and  $\tilde{d}$  is the DDES length scale, which is defined by [40]

$$\tilde{d} = d - f_d \max(0, d - \Psi C_{DES} \Delta), \quad f_d = 1 - \tanh[(8r_d)^3], \quad r_d = \frac{\tilde{\nu}}{|\nabla \mathbf{u}| \kappa^2 d^2}, \quad (3)$$

where  $d$  is the distance to the wall,  $f_d$  is the shielding function,  $\Psi$  the low-Reynolds-number correction function,  $C_{DES} = 0.65$  is the model coefficient,  $\Delta = \max(\Delta x, \Delta y, \Delta z)$  is the measure of grid spacing,  $r_d$  is a dimensionless parameter, and  $\kappa = 0.41$  is the von Kármán constant.

The far-field noise is computed using the FW-H acoustic analogy [44], which adopts an on-body integration of the flow parameters on the blade surface based on the implementation of the Farassat's formulation 1A [45]. After neglecting the quadrupole sound sources and the viscous shear force, the far-field sound pressure can be computed by the superposition of the thickness noise  $p'_T(\mathbf{x}, t)$  and loading noise  $p'_L(\mathbf{x}, t)$ :

$$p'(\mathbf{x}, t) = p'_T(\mathbf{x}, t) + p'_L(\mathbf{x}, t), \quad (4)$$

where  $p'_T(\mathbf{x}, t)$  and  $p'_L(\mathbf{x}, t)$  have the following expressions:

$$4\pi p'_T(\mathbf{x}, t) = \int_{f=0} \left[ \frac{\rho_0 (\dot{U}_n + U_{\dot{n}})}{r(1-M_r)^2} \right]_{\text{ret}} dS + \int_{f=0} \left\{ \frac{\rho_0 U_n [r\dot{M}_r + c_0(M_r - M^2)]}{r^2(1-M_r)^3} \right\}_{\text{ret}} dS, \quad (5)$$

$$\begin{aligned} 4\pi p'_L(\mathbf{x}, t) &= \frac{1}{c_0} \int_{f=0} \left[ \frac{\dot{L}_r}{r(1-M_r)^2} \right]_{\text{ret}} dS + \int_{f=0} \left[ \frac{L_r - L_M}{r^2(1-M_r)^2} \right]_{\text{ret}} dS \\ &+ \frac{1}{c_0} \int_{f=0} \left\{ \frac{L_r [r\dot{M}_r + c_0(M_r - M^2)]}{r^2(1-M_r)^3} \right\}_{\text{ret}} dS. \end{aligned} \quad (6)$$

In the above equations,  $f$  denotes the control surface,  $r = |\mathbf{x} - \mathbf{y}|$  the distance between the observer  $\mathbf{x}$  and the source position  $\mathbf{y}$ ,  $U$  and  $\mathbf{M} = U/c_0$  are the velocity and Mach-number vector of a source point on the integral surface,  $\mathbf{L} = p\mathbf{n}$  is the loading vector, and  $\mathbf{n}$  is the surface unit normal vector.

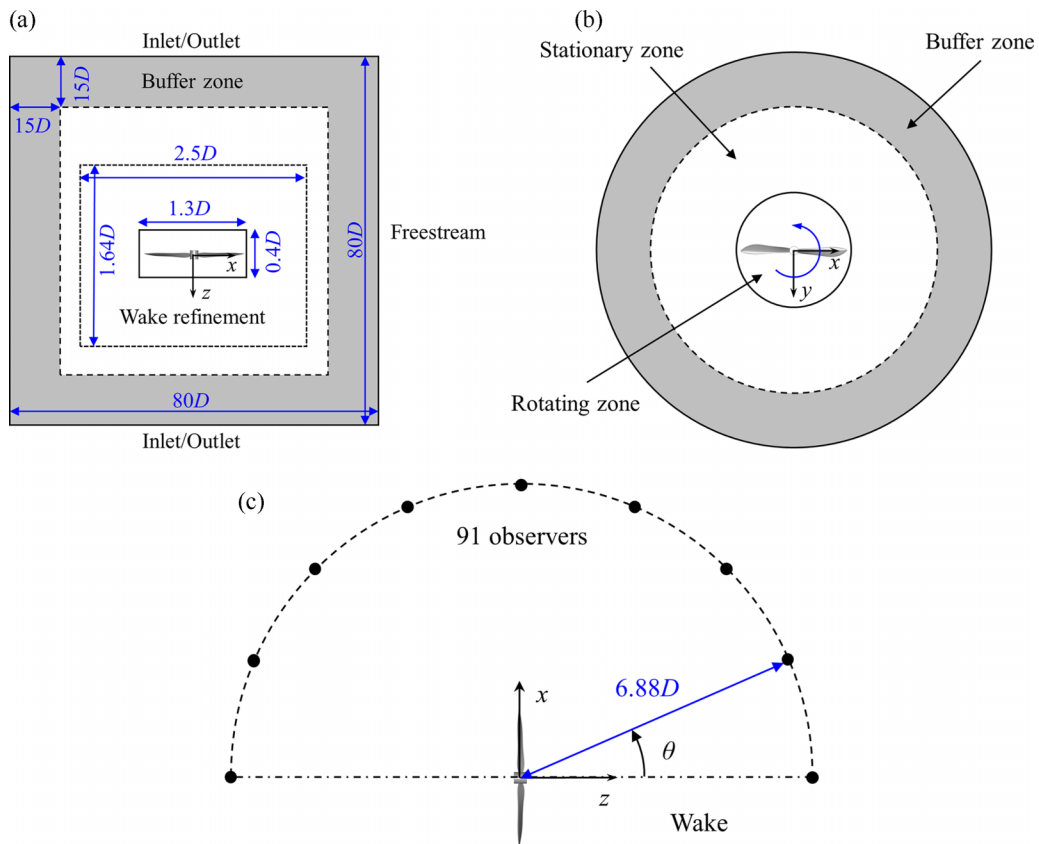


FIG. 3. Schematic of computational setup for simulations (not to scale): (a) side view, (b) top view, and (c) microphone locations. The dotted lines in (a) and (b) show the wake refinement region and the gray area bounded by the dashed line shows the buffer zone.

The subscript  $ret$  denotes that the quantities inside the brackets are evaluated at the retarded time. The subscripts  $r$ ,  $n$ , and  $M$  indicate the projection in the radiation direction, the surface normal direction, and the surface motion direction, respectively. The dot on a variable represents the time derivative.

### B. Simulation setup

Figures 3(a) and 3(b) show the setup of the numerical simulation. The computational domain is a cylindrical volume centered at the rotor with a diameter of  $80D$  and a length of  $80D$ , where  $D = 0.218$  m is the rotor diameter. A cylindrical rotating zone with a diameter of  $1.3D$  and a length of  $0.4D$  is defined around the rotor, in which the grids undergo a prescribed rotating motion along the rotor axis. The sliding mesh technique is used to transfer the information between the two zones through the mesh interface at each time step. Another cylindrical volume around the vehicle with a diameter of  $2.5D$  and a height of  $1.64D$  is the additional refinement region to provide good resolution in the wake region. To minimize the spurious reflection from the boundaries, a buffer zone with a thickness of  $15D$  is adopted.

The rotational speed of the rotor is 90 RPS, corresponding to a blade tip Mach number  $M_{tip} = U_{tip}/c_0 \approx 0.18$ . The total simulation time corresponds to 90 rotor revolutions, and each revolution consists of around 1000 time steps. Ninety-one equally spaced observers are placed within  $180^\circ$  in the  $y = 0$  plane to obtain the noise directivity, as shown in Fig. 3(c). The sampling frequencies for

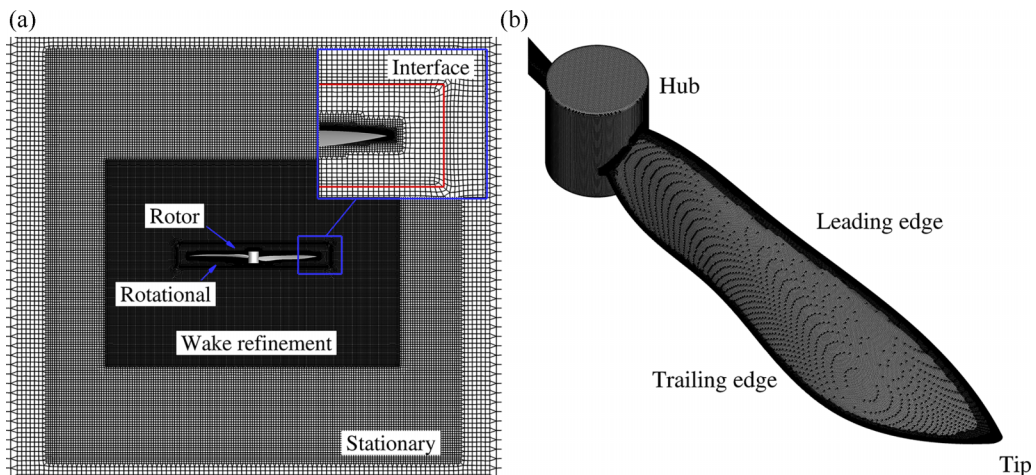


FIG. 4. Computational mesh (a) on  $y = 0$  plane and (b) on the blade surface.

the aerodynamic force and far-field pressure data are 10 and 100 kHz, respectively. The data are sampled after 20 rotor revolutions to ensure the wake flow is fully developed.

### C. Computational grid

Figure 4(a) shows a sectional visualization of the computational mesh. The computational grids comprise 20.3 million cells with hex-core meshing, refined hierarchically approaching the rotor surface. A large wake region is refined to resolve the complex flow structure at VRS and turbulent wake state. Figure 4(b) shows the mesh topology near the propeller surface region. Additional refinement is performed to resolve the sharp trailing edge and to capture the curvature at the leading edge and the blade tip. A grid convergence study is also performed and is presented in Appendix B.

## IV. RESULTS AND DISCUSSION

### A. Experimental results

#### 1. Aerodynamic performance

This section presents the integrated aerodynamic forces measured by the load cell for different rotational speeds and descent rates. Figure 5(a) shows the time-averaged thrust. The thrust at low descent rates shows a higher value than the hovering condition ( $v_d = 0$ ). As  $v_d$  increases, the thrust first shows an increasing trend but soon decreases until a minimum point is reached (7 m/s for 60 RPS, 8 m/s for 70 RPS, and 9 m/s for 80 RPS). As  $v_d$  is further increased, the thrust starts to increase again. Particularly for 60 and 70 RPS, the thrust at high descent rates gradually exceeds that in hovering conditions. The normalized results are shown in Fig. 5(c) to help quantify the relative effect. The hover thrust  $T_h$ , and the corresponding averaged induced velocity under hovering conditions  $v_h$  is used to scale the thrust  $T$  and the rotor descent rate  $v_d$ , respectively. Standard momentum theory [31] gives an induced velocity at the rotor disk by

$$v_h = \sqrt{\frac{T_h}{2\rho_0 A}}, \quad (7)$$

where  $A = \pi D^2/4$  is the disk area. The results for different descent rates are observed to be aligned into a single characteristic curve, which is consistent with the findings in Ref. [39]. The  $T/T_h$  value is slightly larger than 1 within the range of  $v_d/v_h < 1.5$ , but it decreases as the descent rate increases further. The most significant relative thrust loss with a minimum  $T/T_h$  value of about 0.9 is found

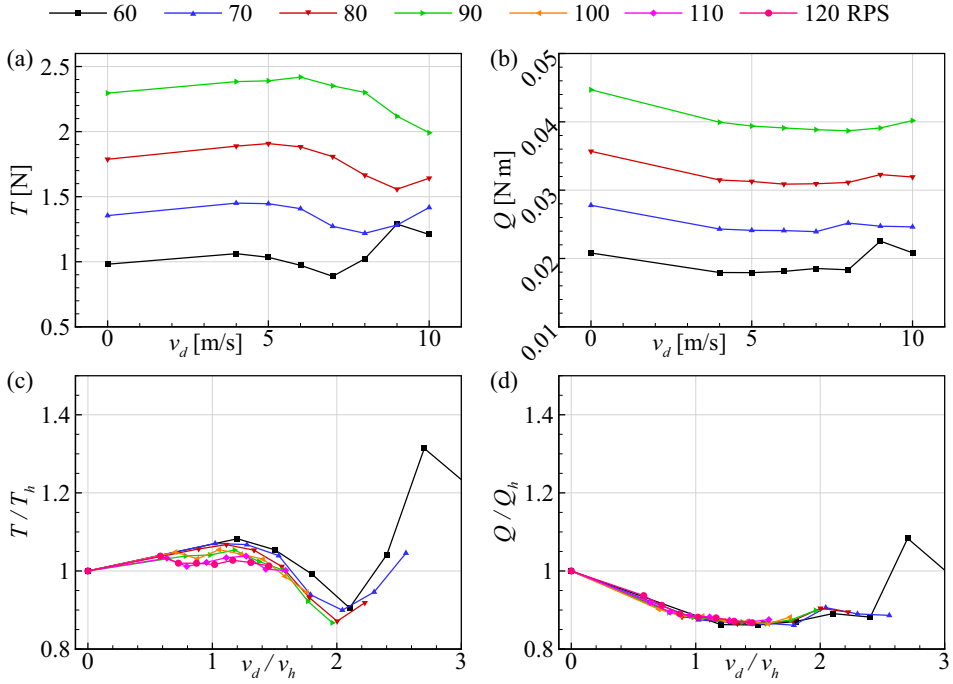


FIG. 5. Measured time-averaged aerodynamic forces over descent rates for different rotational speeds: (a) thrust, (b) torque, (c) normalized thrust, and (d) normalized torque.

at around  $v_d/v_h = 2$ . The thrust deterioration from  $v_d/v_h = 1$  to 2 implies that the rotor might have gradually entered the VRS [32]. Figures 5(b) and 5(d) shows the dimensional and normalized torque results, respectively. Unlike the thrust, the torque shows a monotonic decreasing trend as the descent rate increases until  $v_d/v_h$  reaches a relatively high value. The normalized characteristic curve shows a  $Q/Q_h$  value at around 0.9 over a wide range of  $1 < v_d/v_h < 2.5$ .

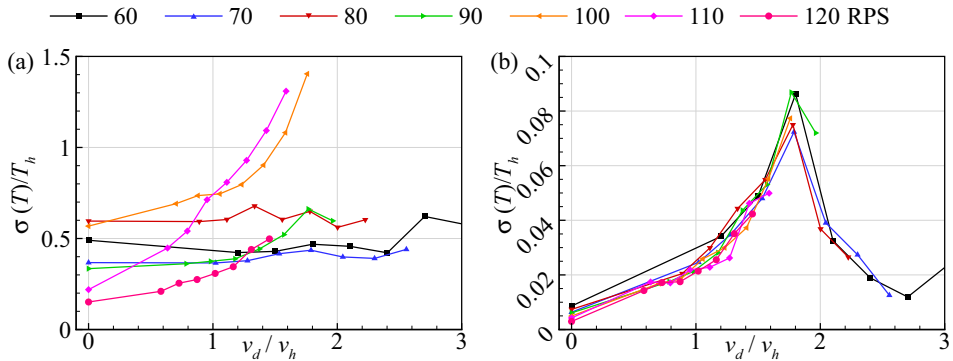


FIG. 6. The standard deviation of the measured thrust signal normalized by hover thrust for different over descent rates for different rotational speeds: (a) raw data and (b) low-pass filtered data with a cut-off frequency of 10 Hz.



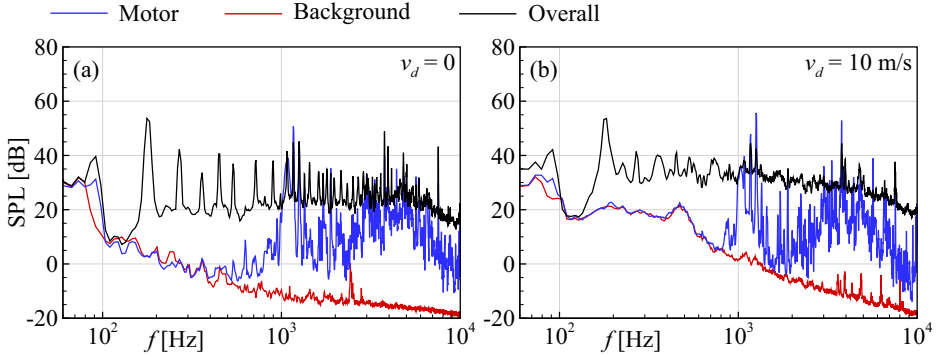


FIG. 7. Measured SPL of different noise sources at two descent rates: (a)  $v_d = 0$  and (b)  $v_d = 10$  m/s. The rotor is working at 90 RPS, and the microphone is located in the rotation plane at  $\theta = 90^\circ$ .

Figure 6(a) shows the normalized standard deviations of the measured thrust time history to quantify the thrust fluctuations at different descent rates. It is computed by

$$\sigma(T) = \sqrt{\frac{1}{t_e - t_0} \int_{t_0}^{t_e} [T(\tau) - \bar{T}]^2 d\tau}, \quad (8)$$

where  $t_0$  and  $t_e$  denote the sampling start and end times, the overbar indicates the time-averaged value. However,  $\sigma(T)/T_h$  exhibits high values across the entire range of the tested descent rates, in which the lowest value is about 0.2 even under hovering conditions and is particularly significant at 100 and 110 RPS. The thrust fluctuations might be attributed to both the mechanical vibrations of the entire test rig and the VRS-induced aerodynamic vibrations. To filter out the low-frequency content of the VRS aerodynamics, we adopt a similar approach to Ref. [38] and apply a low-pass fourth-order Butterworth filter with a cut-off frequency of 10 Hz to the measured thrust signal. According to Ref. [30], the VRS-induced thrust oscillations exhibit a low-frequency feature of a period of 20 to 50 rotor revolutions. Therefore, the cut-off frequency is selected lower than the lowest rotating frequency of 60 RPS, so the high-frequency vibration components induced by rotating motion are filtered out. It is observed from Fig. 6(b) that the filtered normalized standard deviation curves behave similarly and collapses into a single characteristic curve. As the descent rate ratio increases, the normalized thrust standard deviations increase rapidly until reaching peak values at around  $v_d/v_h = 1.7$  and then decrease rapidly. However, the descent ratio for the maximum thrust fluctuation ( $v_d/v_h = 1.7$ ) and the greatest mean thrust loss ( $v_d/v_h = 2.0$ ) do not coincide as previous research states [34,39]. This is possibly attributed to the installation effect of the upstream tower (see Appendix A), which leads to underestimated force measurements. In the ‘‘downstream tower’’ setup, the peaks for maximum mean thrust losses and maximum thrust fluctuations coincide at about  $v_d/v_h = 1.9$  (not shown here), which is consistent with observations from previous research [34,39].

## 2. Aeroacoustic characteristics

This section presents the measured acoustic results from the microphone array. First, the spectra of the facility background noise, the motor noise, and the overall rotor noise at the observer angle  $\theta = 90^\circ$  (please see Fig. 2 for the definition of the observer angle) are compared in Fig. 7. The narrow-band sound pressure level (SPL) is computed as

$$\text{SPL(dB)} = 10 \times \log_{10} \left[ \frac{\text{PSD}(\text{Pa}^2/\text{Hz}) \times \Delta f}{p_{\text{ref}}^2} \right], \quad (9)$$

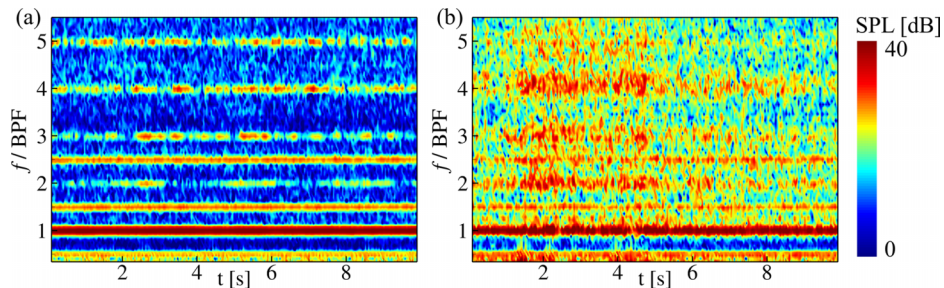


FIG. 8. The spectrograms of SPL at two descent rates: (a)  $v_d = 0$  and (b)  $v_d = 10$  m/s. The rotor is working at 90 RPS, and the microphone is located at  $\theta = 90^\circ$ . The frequency resolution is  $\Delta f = 12.2$  Hz and the time resolution is  $\Delta t = 0.04$  s.

where  $\Delta f = 6.1$  Hz is the frequency resolution,  $p_{\text{ref}} = 2 \times 10^{-5}$  Pa is the reference pressure, and PSD is the power spectra density of the measured acoustic pressure, which is estimated using Welch's method [46] with a Hanning window function and an overlap of 50%. It is observed that good signal-to-noise ratios are achieved for both the lowest ( $v_d = 0$ ) and highest ( $v_d = 10$  m/s) descent rates. The background noise increases with the descent rates, especially in the low-frequency range  $f < 1000$  Hz. The motor noise dominates the distinct tonal peaks at about 1170 and 1260 Hz and also contributes to the broadband components between 3000 to 5000 Hz.

Figure 8 presents the spectrograms in the low-frequency range below 1000 Hz, obtained by performing the short-time Fourier transformation to the acoustic signal. Under hovering conditions, the rotor emits strong tonal noise at the BPF, which keeps a constant acoustic pattern all the time. Other tonal contents occur at harmonics of the BPF, showing a weaker and less continuous pattern than the first BPF tone. It is worth mentioning that there are also tonal peaks at half BPF and its harmonics ( $f/\text{BPF} = 0.5, 1.5, 2.5$ ), showing more continuous characteristics than high-order BPF tones. A discussion of these shaft-order tones can be found in Appendix C. When the rotor experiences a high descent rate, the spectrogram shows a much-scattered shape even for the first BPF tone, indicating a high unsteadiness of the flow around the rotor at high descent rates. Also, the SPL values at multiples of BPF are clearly increased.

Figure 9 shows the noise spectra at both in-plane and out-of-plane observers. Under hovering conditions, multiple tonal peaks can be observed at harmonics of the BPF, especially at the observer angle of  $120^\circ$ , where distinct high-order BPF tones appear between 1000 to 3000 Hz. The high-order BPF tones are explained by some researchers as the effect of the flow recirculation [27]. As the

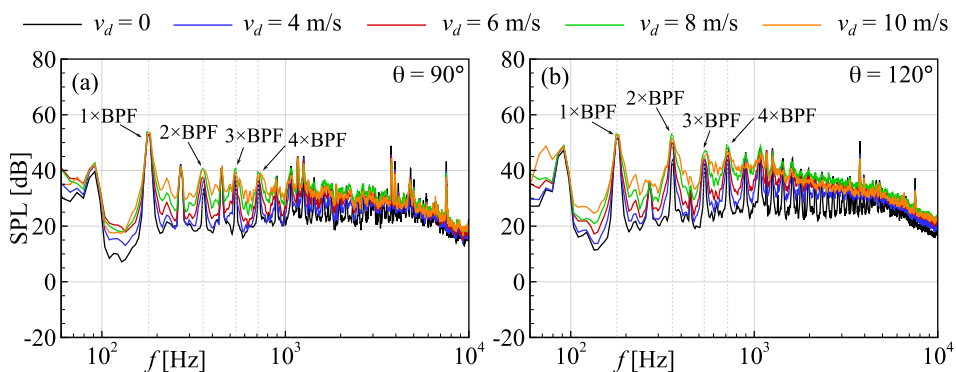


FIG. 9. Comparison of rotor noise over different descent rates at two observer angles: (a) an in-plane observer ( $\theta = 90^\circ$ ) and (b) an out-of-plane observer ( $\theta = 120^\circ$ ). The rotor is operating at 90 RPS.

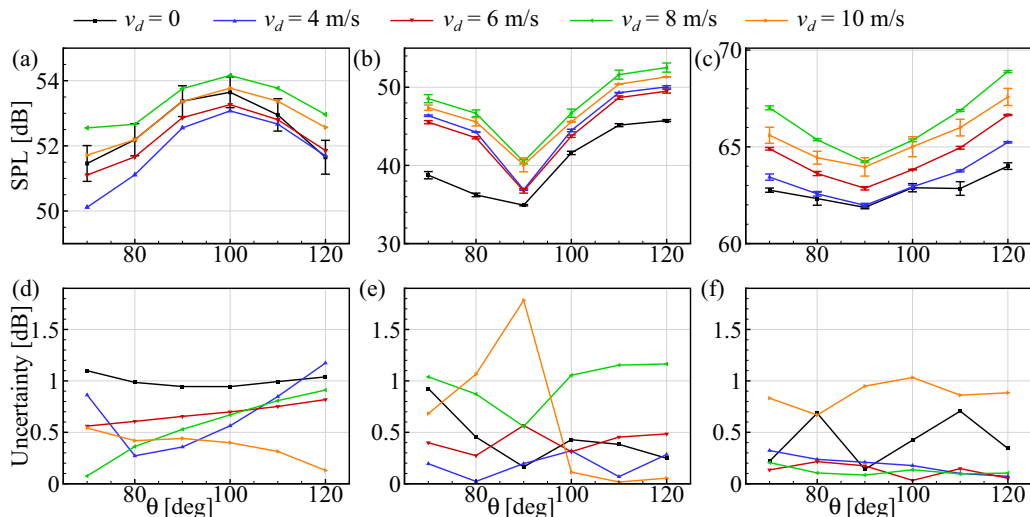


FIG. 10. [(a)–(c)] Sound pressure level for different observer angles (a) at first BPF, (b) at second BPF, and (c) over the whole frequency range between 60 to 10 000 Hz. The error bars indicate the uncertainty from repetitive measurements at the 95% confidence interval. For first BPF only the error bar of  $v_d = 0$  is shown for clarity. [(d)–(f)] The experimental uncertainty at the 95% confidence interval (d) at first BPF, (e) at second BPF, and (f) over the whole frequency range between 60 to 10 000 Hz. The values correspond to the length of error bars in [(a)–(c)]. The rotor is operating at 90 RPS.

descent rate increases, the first BPF tone remains almost unchanged. In contrast, the second BPF tone shows noticeable enhancement, which is more evident for  $\theta = 120^\circ$  shown in Fig. 9(b), where the SPL value at the second BPF tone becomes comparable to the first BPF tone. Another distinctive characteristic is that the spectra are broadened across the whole frequency range, producing spectral humps at multiples of BPFs. The high-order BPF tones are no longer visible at high descent rates, and the spectra gradually exhibit a broadband nature as the descent rate increases. For high-frequency broadband components higher than 5000 Hz, the SPL values are slightly increased and the spectra shapes are unchanged. It is worth mentioning that although the SPL values show an overall increasing trend with the descent rate, at  $v_d = 10$  m/s, both the tonal and the high-frequency broadband components show a lower noise level than at  $v_d = 8$  m/s.

Figures 10(a)–10(c) show the SPL values at all six microphone positions to quantify better the effect of descent rates on the noise directivity. Three repetitive measurements were performed, and the symbols and error bars represent the averaged values and the experimental uncertainties. The experimental uncertainty is calculated based on the  $t$  distribution [47] by

$$u(\text{SPL}) = A \frac{S}{\sqrt{n}}, \quad (10)$$

where  $A = 4.303$  is the constant of a two-sided  $t$  distribution with a sample size of 3 at the 95% confidence interval,  $S$  is the standard deviation of the samples, and  $n = 3$  is the sample size. No significant variation is observed at the first BPF, and the maximum deviation occurs at  $\theta = 70^\circ$  and is within 2 dB, which is small considering the measurement uncertainty for  $v_d = 0$  is about 1 dB. Although the changes due to different  $v_d$  are likely masked by the experimental uncertainty, the SPL at first BPF shows similar directivity for different  $v_d$ . In contrast, the second BPF tone experiences a significant enhancement at all observer angles, particularly in the upstream and downstream directions. An overall increase of about 10 dB can be observed at  $v_d = 10$  m/s. The overall sound pressure level (OASPL) shown in Fig. 10(c) demonstrates a relatively even increase

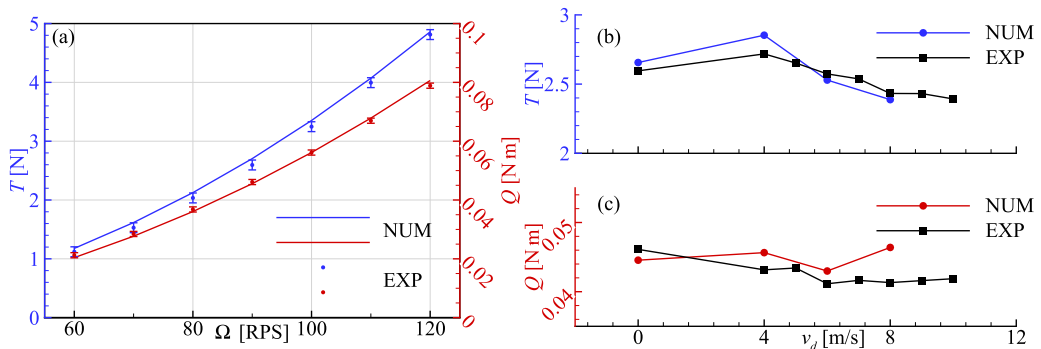


FIG. 11. (a) Thrust and torque comparison between steady simulations and experimental results for hovering rotor operating at different rotational speeds. The uncertainty are obtained from repetitive measurements at the 95% confidence interval [25]. (b) Thrust and (c) torque comparison between the time-averaged results in transient simulations and experimental results for rotor operating at 90 RPS and different descent rates. The measured force results shown here are from the “downstream tower” case (see Appendix A).

with the descent rates, which can be up to 4 dB at  $v_d = 10$  m/s. The noise level reduction from  $v_d = 8$  m/s to  $v_d = 10$  m/s possibly implies the gradual disappearance of the unsteady VRS, which will be further analyzed using the flow field results in the next section.

Figures 10(d)–10(f) shows the corresponding measurement uncertainty values for direct quantification of the error bar length that may not be easy to distinguish. For most observer angles  $\theta$  and descent rates  $v_d$ , the uncertainty is within 1 dB, indicating good repeatability of current experiments.

## B. Numerical results

The experimental results presented so far show how the descending flight affects the aerodynamic and aeroacoustic performance of the rotor. However, analyzing the corresponding mechanisms requires more detailed information, such as the near-field flow structures and on the rotor blade surface. In this section, we will present the results of numerical simulations to provide physical insights for understanding the relevant aerodynamic and aeroacoustic effects.

### 1. Aerodynamic performance

First, steady Reynolds-averaged Navier-Stokes (RANS) simulations are performed to validate the numerical model at different rotational speeds at a reasonable cost. Figure 11(a) compares the simulated aerodynamic forces with the experimental measurements for the rotor in hovering conditions. It is observed that nearly all the simulated results fall within the error bars of the experiments across the operating rotating speeds, indicating a good simulation accuracy. Since the RANS model can only provide mean aerodynamic results, transient DDES computations are then performed at 90 RPS. Four descent rates of  $v_d = 0, 4, 6,$  and  $8$  m/s are simulated and compared. Figures 11(b) and 11(c) compares the thrust and torque results in transient simulations and experiments. The computed results show a relatively good agreement with the experiments, except for some overprediction in the torque computation at high descent rates.

### 2. Flow field

In this section, we study the influence of the descending flight on the near-field flow structure. Figure 12(a) presents the isosurfaces of the instantaneous  $Q$  criterion at the four descent rates. Under the hovering condition, tip vortices shed from the two blades and are convected downstream following a helicoidal path. However, after about one rotor revolution, the top vortices are gradually distorted and broken into small structures. In contrast, the hub vortices show a more persistent

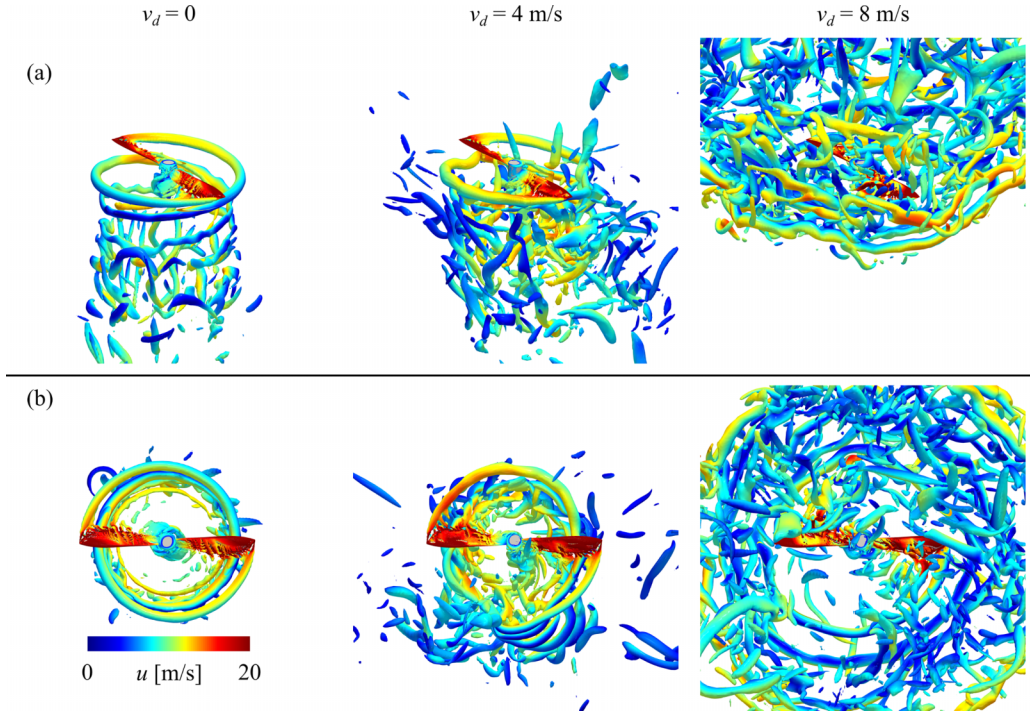


FIG. 12. Instantaneous flow structures shown by  $Q = 200\,000\text{ s}^{-2}$  isosurfaces colored by velocity magnitude at the last rotor revolution: (a) three-dimensional view and (b) top view. From left to right:  $v_d = 0, 4,$  and  $8$  m/s. The rotor is operating at 90 RPS.

spiral precession than the tip vortices. There are also visible small-scale vortex structures shed from the suction side of the blade surface. As the descent rate increases to  $v_d = 4$  m/s, The tip vortices exhibit more deformed shapes and break down faster, producing a complicated turbulent wake downstream of the rotor. Small vortical structures are observed outside the clearly defined rotor stream tube in hover and are blown upstream at high descent rates, which is more profound at  $v_d = 8$  m/s where the wake locates above the rotor. Figure 12(b) provides the top view of the vortex structures. One distinctive feature is that the wake dispersion becomes spread as the descent rate increases, leading to a radially expanded tip vortices trajectory rather than a contracted rotor wake profile as in hover condition.

Figure 13(a) provides the contour plot of the phase-averaged axial velocity  $\langle u_z \rangle$  superimposed with streamlines at different descent rates. The phase-average quantities are computed by averaging over the results at the same revolving phase such that the number of sampled fields equals the number of rotor revolutions. In hover, the flow acceleration along the streamlines and the rotor wake contraction are clearly shown. At  $v_d = 4$  m/s, a smaller downwash region is observed. The rotor wake slightly spreads outwards, resulting in vortices in the downstream wake where shear layers are formed due to the opposite descent velocity to the wake velocity. As the descent rate further increases to 8 m/s, the vortical structures are shifted upstream and begin to envelop the rotor tip. The velocity direction below the rotor is reversed, and the wake moves above the rotor. The recirculation zone around the rotor tip forms a clear toroidal structure, showing typical VRS characteristics.

Figure 13(b) shows the phase-averaged velocity magnitude profile at three different locations [marked by dashed lines in Fig. 13(a)] in the rotor wake. For the hovering condition, the induced velocity in the immediate vicinity of the rotor ( $z/R = 0.25$ ) is low near the rotor hub and tip

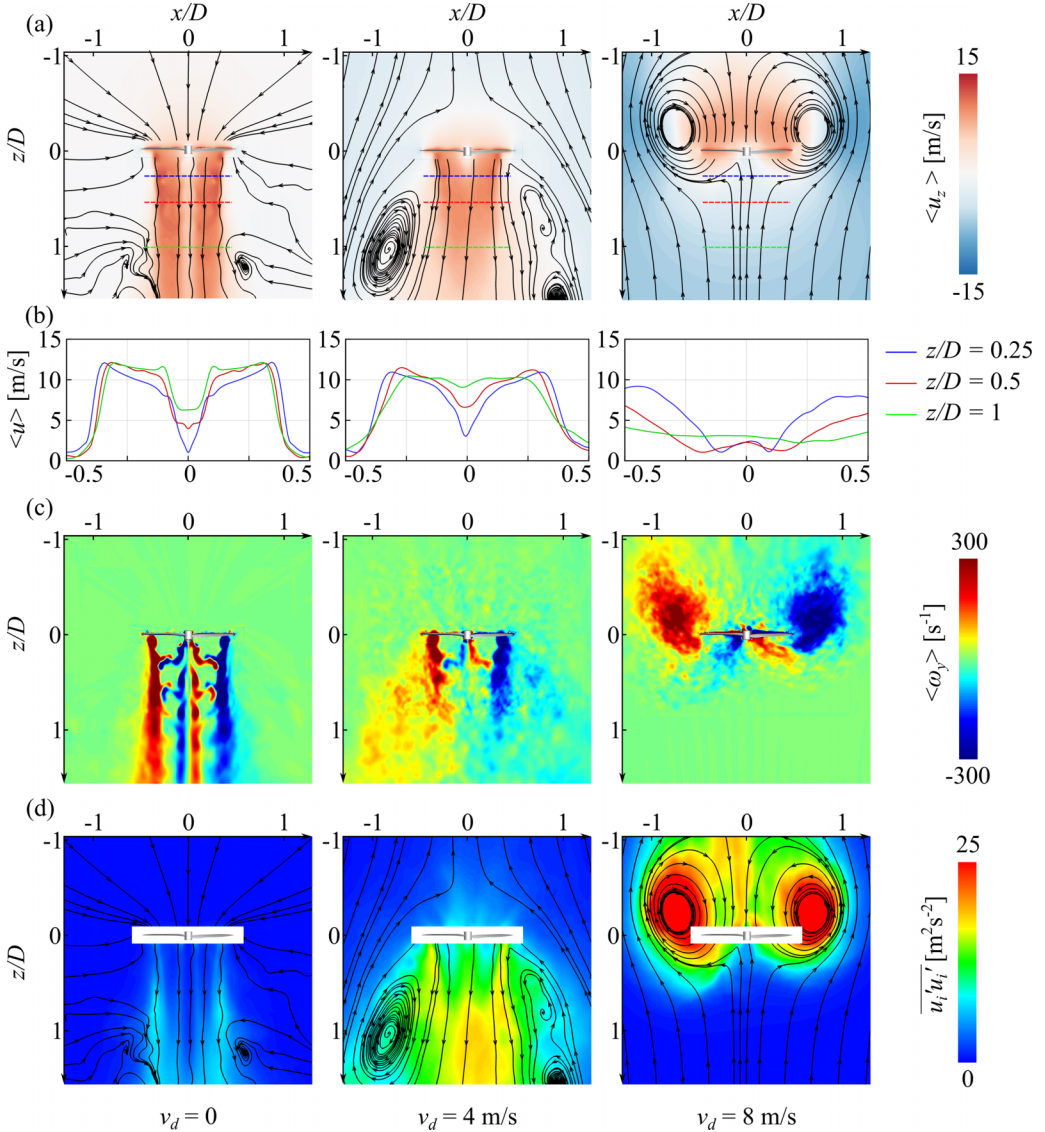


FIG. 13. The contour of (a) phase-averaged axial velocity, (c) phase-averaged vorticity in  $y$  direction, and (d) turbulent kinetic energy with descent rate  $v_d$  from 0 to 8 m/s at  $y = 0$  slice. From left to right:  $v_d = 0$ , 4, and 8 m/s. The streamlines shown in (a) and (d) are based on the phased-averaged velocity field. (b) The phase-averaged velocity profile along probing lines at  $z/R = 0.25, 0.5$ , and 1. The rotor is operating at 90 RPS.

while showing high values elsewhere. The profiles become more uniform as the flow proceeds downstream. As  $v_d$  increases to 4 m/s, the velocity becomes more evenly distributed along the rotor span, especially at the hub downstream locations, implying a stronger momentum mixing in the rotor wake region. At  $v_d = 8$  m/s, the velocity profile shows a different shape with a larger velocity at the blade tip than at the hub due to the reversed flow direction.

Figure 13(c) shows the contour plot of the phase-averaged vorticity in the  $y$  direction. During hovering, strong vortices shed from the blade tips and hub, propagating downstream and interacting with each other. At  $v_d = 4$  m/s, the far wake shows evidence of dispersion and spreads toward the radial direction. The hub vortices become less visible, and the tip vortices are distorted. At

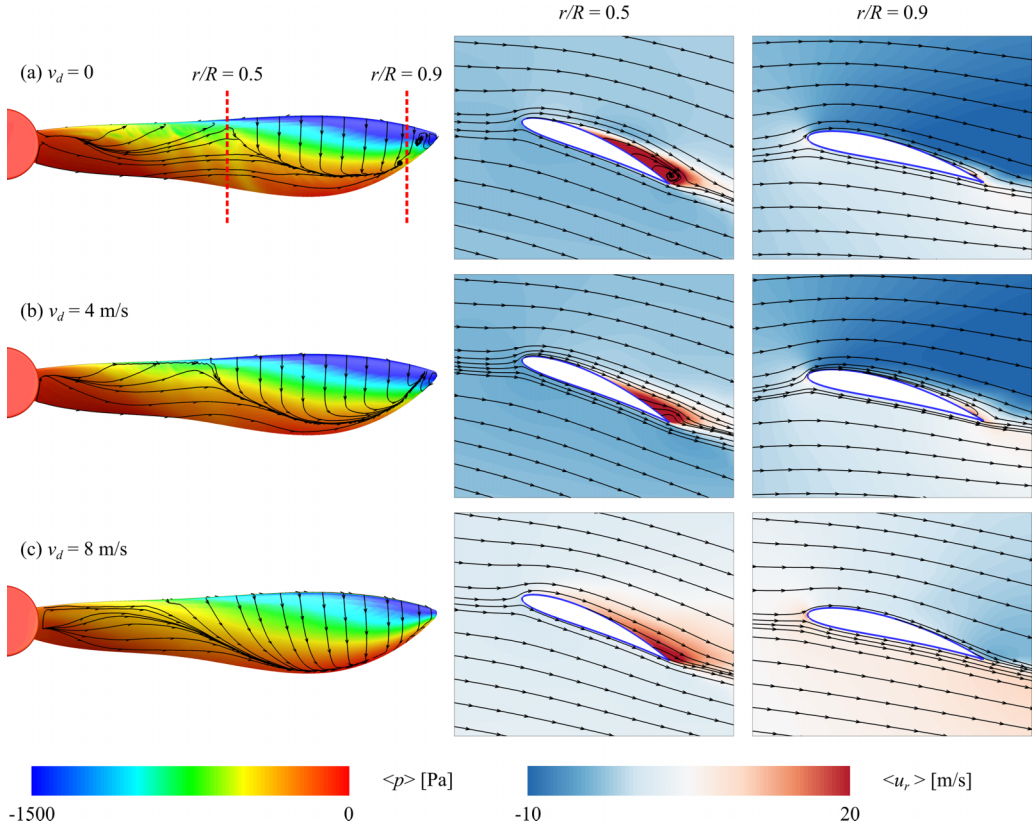


FIG. 14. Left: Phase-averaged limiting streamlines superimposed with phase-averaged gauge pressure contour on blade suction surface. Right: Sectional streamlines based on relative velocity superimposed with phase-averaged radial velocity contour at  $r/R = 0.5$  and  $0.9$ . From top to bottom the results are from different descent rates: (a)  $v_d = 0$ , (b)  $v_d = 4$  m/s, and (c)  $v_d = 8$  m/s. The rotor is operating at 90 RPS.

$v_d = 8$  m/s, the tip vortices accumulate around the blade tips, forming a representative toroidal vortex structure immediately above the blade tips, which indicates a fully developed VRS topology. Further insights into the turbulent kinetic energy (TKE) field are presented in Fig. 13(d). Low values of TKE are found along the tip vortices trajectory for the hovering condition, whereas the TKE becomes higher as  $v_d$  increases to 4 m/s, showing an apparent radial diffusion. At higher descent rates at  $v_d = 8$  m/s, the TKE is mainly concentrated within the vortex ring, which indicates stronger velocity fluctuations are experienced by the rotor when entering the VRS.

Figure 14 introduces the flow field near the rotor blade. The phase-averaged limiting streamlines [48] overlaid with the phase-averaged gauge pressure is shown on the left side to help analyze the flow structure on the blade suction surface. The phase-averaged limiting streamlines are based on the wall shear stress computed from the phase-averaged relative velocity  $\langle \mathbf{u} \rangle_r$ .  $\langle \mathbf{u} \rangle_r$  is computed by subtracting the rotational velocity from the flow velocity, i.e.,  $\langle \mathbf{u} \rangle_r = \langle \mathbf{u} \rangle - \boldsymbol{\Omega} \times \mathbf{y}$ , where  $\boldsymbol{\Omega}$  and  $\mathbf{y}$  are the rotor angular velocity and the coordinate vector, respectively. At  $v_d = 0$ , the flows smoothly move in the circumferential direction in the high  $r/R$  region and occupy about half the blade area, whereas strong radial flows can be observed in the low  $r/R$  region. The streamlines are aggregated near the trailing edge, driving the fluid from the blade root to the tip. When the descent rate increases, the aggregated streamlines move towards the trailing edge, forming a larger area of smooth flows. The pressure distribution in hover presented in Fig. 14(a) shows a clear adverse pressure gradient along the chord, especially near the tip. With the increase of  $v_d$ , the pressure near the leading edge increases, resulting in thrust loss, as presented in the last section.

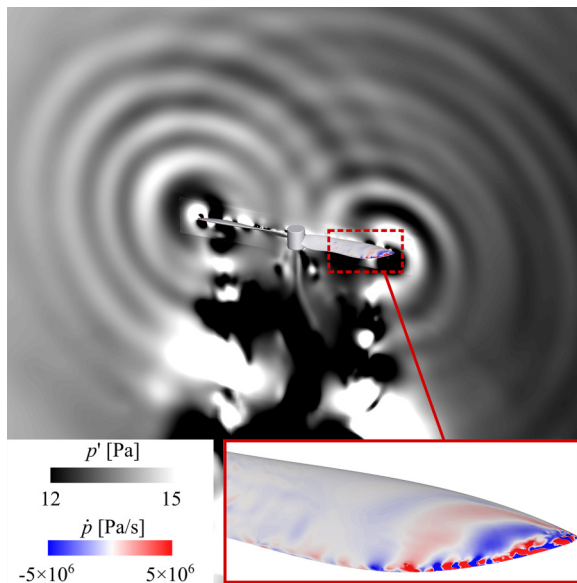


FIG. 15. Sound pressure  $p'$  field at  $y = 0$  slice and instantaneous pressure time derivative  $\dot{p}$  on the blade surface of a hovering rotor at 90 RPS.

Figure 14 also shows the flow field at different radial sections, presented by the projection of the phase-averaged streamlines overlaid with the radial phase-averaged velocity contour. At  $r/R = 0.5$ , a visible separation bubble is observed near the trailing edge when  $v_d = 0$ , accompanied by strong radial flows. The increase in the descent rate leads to more attached streamwise flows and larger area of radial flows. Compared to  $r/R = 0.5$ , the streamwise flow at  $r/R = 0.9$  is more smooth and attached due to the higher rotational speed and lower angle of attack, with much weaker radial flows  $r/R = 0.5$ . At  $v_d = 8$  m/s. It is noted that the radial velocity towards the blade tip direction increases for both pressure and suction sides of the blade, which could be explained by the additional spanwise velocity induced by the vortex ring whose core locates above the rotor.

### 3. Aeroacoustic characteristics

This section presents the far-field acoustic prediction and relevant noise source analysis based on computed near-field flow data. Figure 15 shows the acoustic pattern radiated from a hovering rotor at a rotational speed of 90 RPS. The pressure fluctuation  $p'$  is defined by subtracting the phase-averaged pressure  $\langle p \rangle$  from the computed instantaneous pressure  $p$ . It seems that the radiated noise mainly comes from the blade tip region. Also, the time derivative of the pressure on the blade surface, one of the terms in Eq. (6), is presented in Fig. 15. It is found that the blade trailing edge and the tip is the primary  $\dot{p}$  source location in hovering conditions.

First, the numerical model is validated with the experimental measurements. Figures 16(a) and 16(b) compare the sound spectra of the hovering rotor at 90 RPS between the simulation and experimental results. As mentioned in Sec. II B, a wind tunnel which contains an outlet and flow collector is used in this work. While other parts are either installed with perforated plates or covered by sound-absorbing foams, the noise scattering from the tunnel outlet and collector might influence the noise measurements. Therefore, here we also include the results from our previous measurements [25], which were performed in a fully anechoic chamber to exclude the influence of the tunnel test section. At the in-plane observer [ $\theta = 90^\circ$ , Fig. 16(a)], the spectra below 1000 Hz show similar shapes and noise levels for both anechoic chamber and wind tunnel configuration, except that some additional tonal peaks occur when the tunnel test section exists. This additional high-order BPF



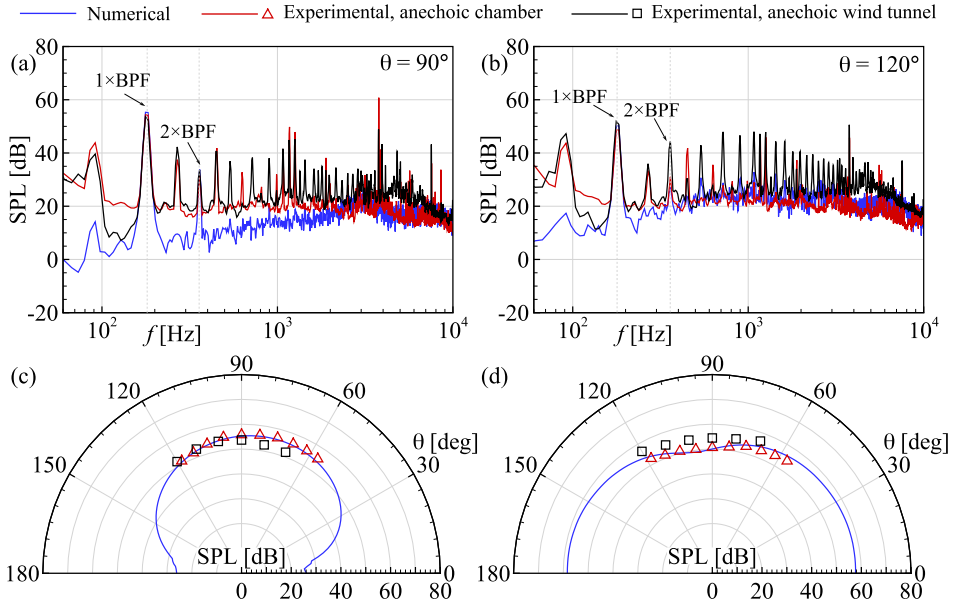


FIG. 16. Comparison between the numerical simulations, the experimental measurements from the anechoic chamber and the anechoic wind tunnel. Noise spectra at observer angles of (a)  $\theta = 90^\circ$  and (b)  $\theta = 120^\circ$ . Noise directivity of (c) the first BPF tone and (d) the OASPL of the broadband noise between 1000 and 10 000 Hz. The broadband noise for OASPL calculation in (d) is smoothed using a moving average filter. The rotor is in hover and rotates at 90 RPS.

harmonic content is likely caused by the flow recirculation effect [27,49] because the anechoic chamber data are sampled in a short time before the flow recirculation is established, whereas the wind tunnel data are sampled after a settling time to ensure the relevant vortex ring structures are well developed. At  $f > 1000$  Hz, the results of wind tunnel tests show a higher level of broadband noise across the frequency range up to 10 000 Hz, which possibly results from the noise scattering effect by the present of the tunnel outlet and collector. The simulation successfully captures the first and second BPF tones while underestimating the broadband components below 2000 Hz. For higher frequency range  $f > 2000$  Hz, the simulation agrees well with the anechoic chamber test, in which the possible reflections are avoided. At the out-of-plane observer [ $\theta = 120^\circ$ , Fig. 16(b)], the additional tonal peaks of the wind tunnel results are even more significant over frequency up to 5000 Hz compared to the anechoic chamber results. The simulated spectrum shows a good agreement with the anechoic chamber measurements over the whole frequency range. Figures 16(c) and 16(d) present the noise directivity plot of the first BPF tone and the OASPL of the broadband noise between 1000 and 10 000 Hz, respectively. At the first BPF, the simulated directivity matches well with the anechoic chamber results. In contrast, the SPL of wind tunnel results show slightly lower values, possibly related to the thrust loss caused by the upstream tower installation, which will be discussed in Appendix A. The OASPL of the broadband noise for the wind tunnel results shows some discrepancies within 4 dB at all observer angles. Generally, the simulations show encouraging agreement with experiments, and the presence of the tunnel outlet and collector can significantly increase the broadband noise level. Nevertheless, this does not affect the following discussions, as we are concerned with the relative changes due to the descending speed.

Figures 17(a) and 17(b) compare the simulated acoustic spectra at different descent rates. As  $v_d$  increases, the most remarkable change is the presence of the humps at multiples of BPF. The spectral broadening effect is observed in the frequency range of less than 3000 Hz, and the corresponding SPL values show similar amplitudes compared to the experimental results in Fig. 9. However, the

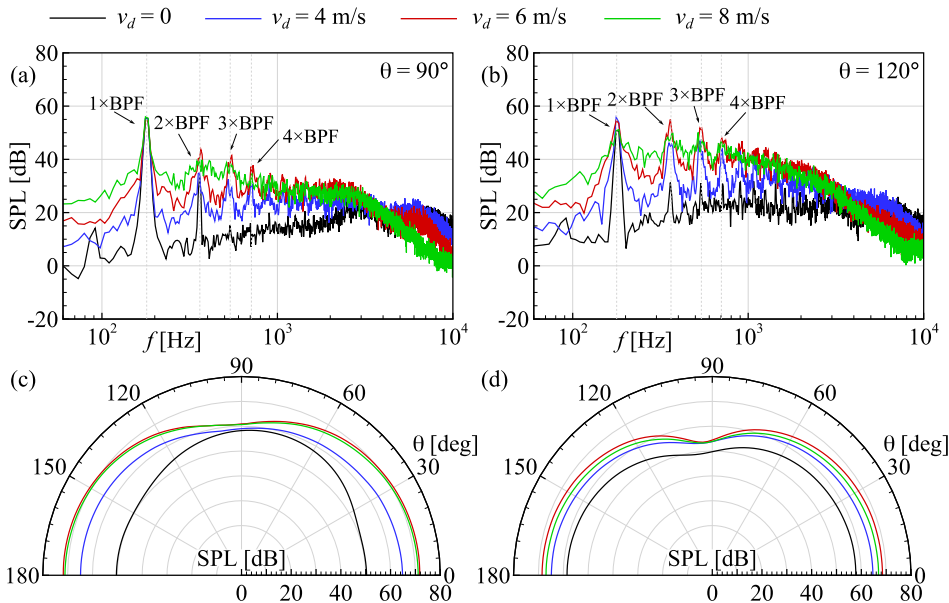


FIG. 17. Simulated far-field noise data at different descent rates. Noise spectra at observer angles of (a)  $\theta = 90^\circ$  and (b)  $\theta = 120^\circ$ . Noise directivity of (c) the OASPL between 100 Hz and 1000 Hz and (d) the OASPL between 1000 and 10 000 Hz. The rotor rotates at 90 RPS.

high-frequency broadband noise shows a certain level of underprediction, especially at high descent rates. This discrepancy is attributed to incorrect boundary layer computations such that the high-frequency pressure fluctuation on the blade surface is not fully resolved. Also, the SPL values for  $v_d = 8$  m/s are slightly less than  $v_d = 6$  m/s for  $f > 1000$  Hz, while the corresponding descent rate for the noise level to start decreasing occurs between  $v_d = 8$  m/s and  $v_d = 10$  m/s in the experiments. Figures 17(c) and 17(d) show the OASPL directivity in the frequency range of  $60 \text{ Hz} < f < 1000 \text{ Hz}$  and  $1000 \text{ Hz} < f < 10\,000 \text{ Hz}$ , respectively. It can be seen that with the increase of the descent rate, the radiated noise is intensified at all observer angles until  $v_d$  reaches 8 m/s, where the SPL values show a slight decrease. The additional noise at low frequencies mainly emits in the upstream and downstream directions, whereas the high-frequency broadband noise shows a more uniform enhancement in all directions. In general, the findings from the simulations are consistent with the experimental observations presented in Figs. 9 and 10.

To have a holistic perspective on the noise characteristics, we present the noise spectra contour in Fig. 18, which clearly shows the directivity pattern at  $f/\text{BPF} \leq 5.5$ . In hover, a strong tone occurs at BPF, with several weaker tones at BPF harmonics. The radiation for the first BPF tone is strongest in the rotation plane, while higher-order BPF tonal noise radiates perpendicular to the rotation plane. As the descent rate increases, additional noise that mainly radiates upstream and downstream is produced around multiples of BPF, and the acoustic energy near the BPF tones spreads to nearby frequencies.

An aeroacoustic source analysis is performed to help explain the relevant physical mechanisms for the aforementioned noise generation, and the on-surface distributions of the unsteady loading noise sources are presented. Figures 19(a), 19(c) and 19(e) show the root mean square of the pressure  $p_{\text{rms}}$  on both suction and pressure sides, which stands for the distribution of the pressure fluctuations. For the rotor in hover, high  $p_{\text{rms}}$  is found in a small region on the suction surface, located at the leading edge and the trailing edge near the blade tip. At  $v_d = 4$  m/s, much stronger pressure fluctuations at the blade leading edge are observed, which is even more pronounced if the descent rate is further increased to  $v_d = 8$  m/s. The results suggest that the blade's leading edge could be

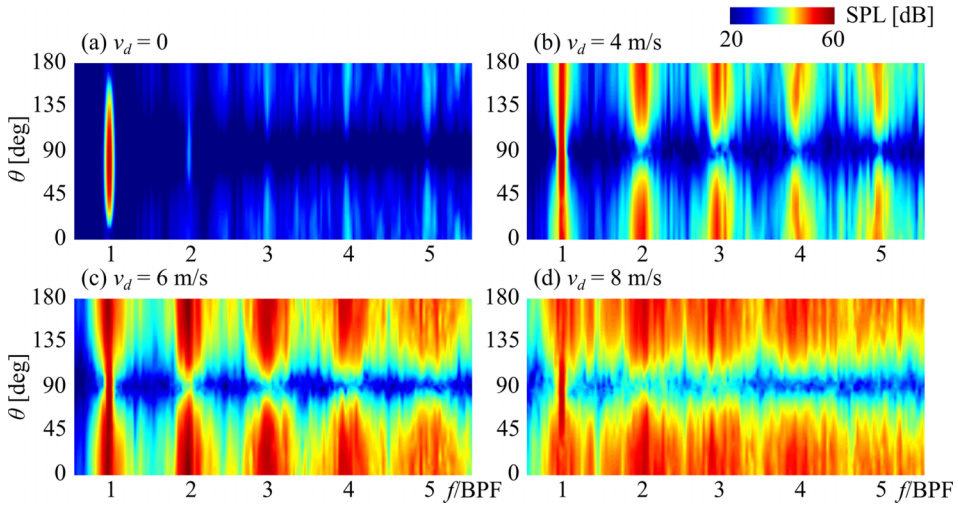


FIG. 18. Contour plot of noise spectra in various radiation directions at different descent rates. The horizontal coordinate: normalized frequency by BPF; the vertical coordinate: observer angle. The rotor is operating at 90 RPS.

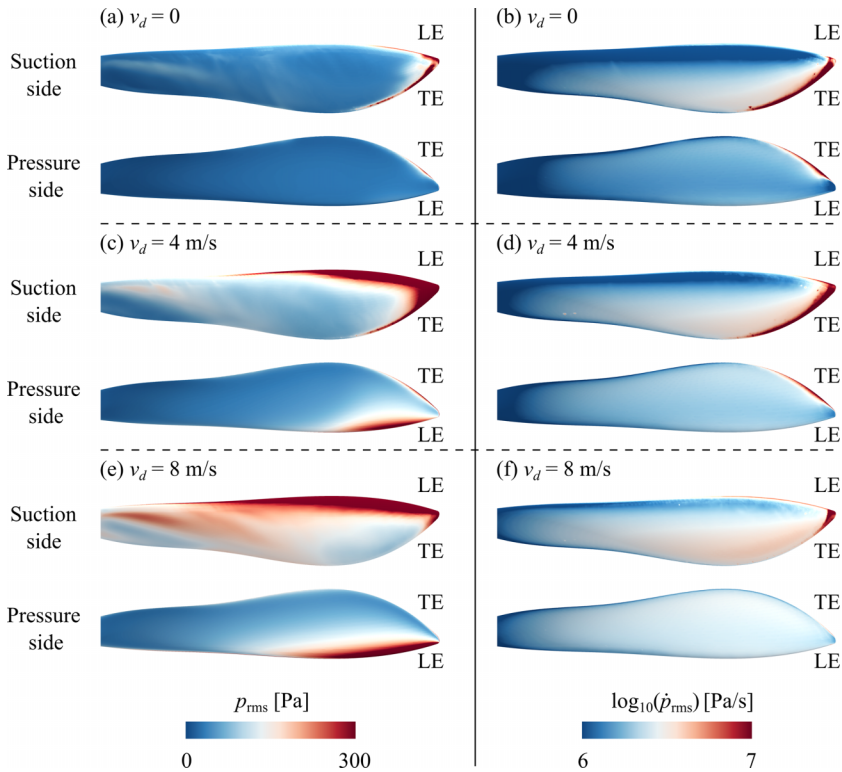


FIG. 19. Contour of the root mean square of the surface pressure  $p_{\text{rms}}$  and its the time derivative  $\dot{p}_{\text{rms}}$  field on both suction and pressure surfaces for rotor at different descent rates: [(a) and (b)]  $v_d = 0$ , [(c) and (d)]  $v_d = 4$  m/s, and [(e) and (f)]  $v_d = 8$  m/s. The abbreviations “LE” and “TE” represent leading edge and trailing edge, respectively. The rotor rotates at 90 RPS.

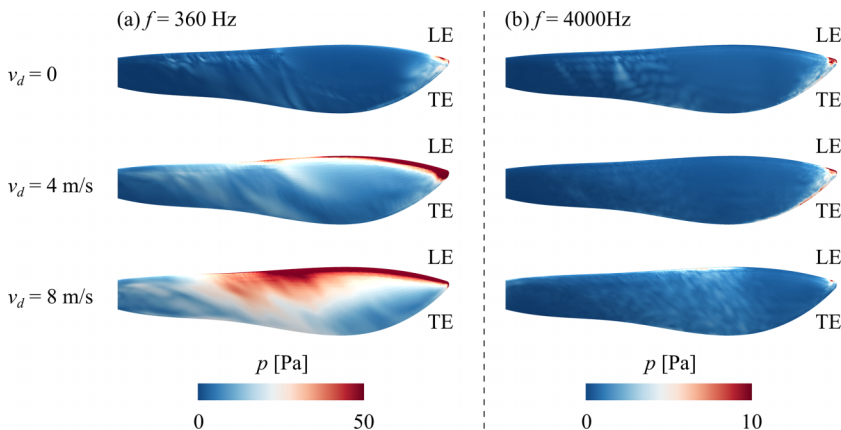


FIG. 20. Distribution of blade surface pressure field  $p$  at two different frequencies: (a)  $f = 360$  Hz and (b)  $f = 4000$  Hz. Only results on blade suction surface are shown for clarity. The rotor rotates at 90 RPS.

the dominant noise source in descent flight, in which the vortex structures in the rotor wakes are blown to the rotor plane, as shown in Figs. 12 and 13. Thus, the vortex structures are likely cut by the rotating blade, causing significant leading edge noise that is broadband in nature. Also, the coupling with the rotational process can also lead to the so-called haystacking-like characteristics as explained in Ref. [50]. The pressure fluctuations on the pressure side show a similar response to the suction side. Figures 19(b), 19(d) and 19(f) shows the root-mean-square distribution of the surface pressure time derivative  $\dot{p}_{\text{rms}}$ , which has also been adopted in many aeroacoustic studies [11, 51, 52] for noise source analysis. At  $v_d = 0$ , the dominant sources are mainly distributed at the blade's trailing edge, which is observed on both sides. The distributions are generally similar for  $v_d = 0$  and  $v_d = 4$  m/s, whereas, for a higher descent rate at  $v_d = 8$  m/s, the  $\dot{p}$  source at the leading edge becomes slightly stronger.

The frequency properties of the aeroacoustic sources are presented using a similar method as Ref. [53] to better correlate the surface noise sources with the far-field noise. Figure 20 shows the frequency-domain  $p(\mathbf{x}, f)$  source on the blade surface, which is computed by taking a Fourier transform to the time-domain source  $p(\mathbf{x}, t)$ . A total of 20 000 blade surface snapshots were stored, corresponding to 18 rotor revolutions. The Fourier transform results are obtained using a block averaging method with a Hanning window function and an overlap of 50%. The resulting frequency resolution is  $\Delta f \approx 30$ . Two representative frequencies,  $f = 360$  and 4000 Hz, are compared for different descent rates. The former corresponds to the second BPF tone at which the effect of the descent flight has the most significant impact, and the other represents a typical frequency in the broadband range. At the second BPF, most of the sources on the suction surface are weak except for a small region near the tip. As the descent rate increases to 4 m/s, strong sources appear at the leading edge, covering the outer half of the rotor span. At  $v_d = 8$  m/s, the sources at the leading edge extend towards the root and the middle of the blade. In contrast, the surface pressure component at  $f = 4000$  Hz mainly occurs at the blade tip, and the  $p$  source distribution for the three descent rates does not show a significant difference. It should be noted that the contours in Figs. 20(a) and 20(b) are plotted with different scales, which means the  $p$  sources show much less contribution at  $f = 4000$  Hz than at  $f = 360$  Hz.

Figure 21 shows the distribution of the surface pressure time derivative  $\dot{p}$ . At the second BPF, the dominant sources are still located at the tip region, and significant sources appear at the leading edge when the rotor descends, showing a similar trend as the  $p$  source distribution. However, at  $f = 4000$  Hz significant  $\dot{p}$  sources appear at the trailing edge rather than at the leading edge, indicating that the significant noise sources in the high-frequency broadband range come from the blade trailing edge noise. The results for  $v_d = 0$  and 4 m/s show similar source distribution, while  $v_d = 8$  m/s

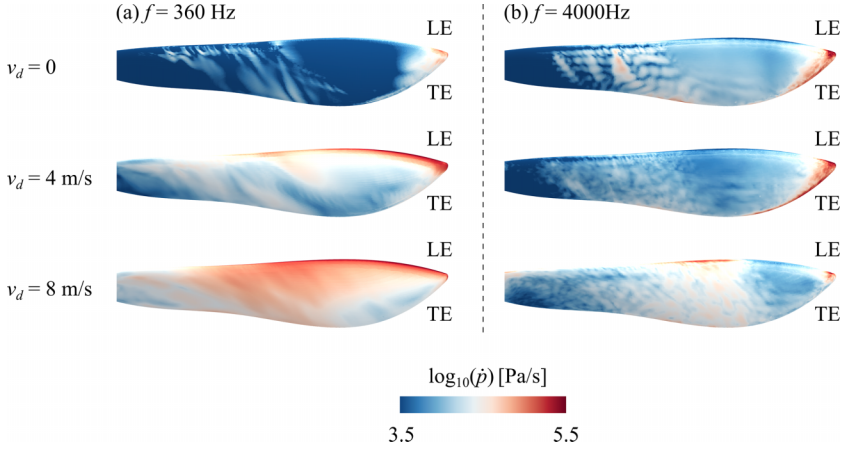


FIG. 21. Distribution of blade surface pressure time derivative field  $\dot{p}$  at two different frequencies: (a)  $f = 360$  Hz and (b)  $f = 4000$  Hz. Only results on blade suction surface are shown for clarity. The rotor rotates at 90 RPS.

shows a slight increase at the blade leading edge. It is also observed that the trailing edge sources become weaker at  $v_d = 8$  m/s, which is possibly attributed to the limitation of current numerical models to accurately resolve the boundary layers when the nearfield flow is complex and highly unsteady, which leads to an underprediction of the SPL values at high frequencies, as observed in Fig. 17.

A blade-to-blade correlation analysis is performed to justify the inference that the additional noise is caused by rotor blades' successive cutting of the same turbulence structures in the rotor's own wake. The blade-to-blade correlation coefficient is defined as [6]

$$r_{p'} = \frac{\mathbb{E}[p'(\mathbf{x}_1, t)p'(\mathbf{x}_2, t + \pi/\Omega)]}{\sqrt{\mathbb{E}[p'^2(\mathbf{x}_1, t)]}\sqrt{\mathbb{E}[p'^2(\mathbf{x}_2, t + \pi/\Omega)]}}, \quad (11)$$

where  $p'(\mathbf{x}_1, t)$  represents the time history of the pressure fluctuation at a certain location  $\mathbf{x}_1$  on the surface of one blade,  $p'(\mathbf{x}_2, t + \pi/\Omega)$  is the pressure fluctuation at the corresponding point  $\mathbf{x}_2$  of the other blade such that  $\mathbf{x}_1$  and  $\mathbf{x}_2$  has a phase difference of  $\pi$ , and the operator  $\mathbb{E}[\cdot]$  indicates the expected value. Figure 22 presents the blade-to-blade correlation coefficients along different testing

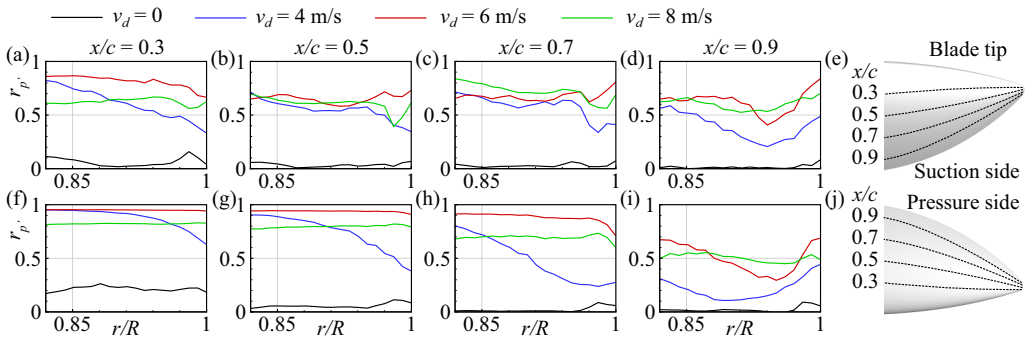


FIG. 22. Blade-to-blade correlation coefficients of  $p'$  at four different lines near the blade tip: [(a) and (f)]  $x/c = 0.3$ , [(b) and (g)]  $x/c = 0.5$ , [(c) and (h)]  $x/c = 0.7$ , and [(d) and (i)]  $x/c = 0.9$ . Definition of the testing lines: (e) suction side and (j) pressure side. [(a)–(d)] The suction side and [(f)–(i)] the pressure side.

lines at the blade tip. The blade-to-blade correlation is weak in hovering conditions on both suction and pressure sides, and it increases with the descent rate. This indicates that the flow structures experienced by the blade tip become more similar when the vortex ring is formed. It is also observed that the blade-to-blade correlation is slightly stronger near the leading edge than near the trailing edge, which is reasonable because the interaction between the blade tip and the turbulent structures starts from the leading edge.

## V. CONCLUSION

The aerodynamics and the aeroacoustics of a drone rotor in axial descending flight are investigated experimentally and numerically. The results of experimental measurements, including integrated aerodynamic forces and microphone data, are first presented and compared. The rotor experiences a slight mean thrust increase at low descent rates but a mean thrust loss of up to 10% at high descent rates. On the contrary, a more uniform decrease of about 10% in torque is observed across a wide descent rate range. Strong thrust fluctuations are found with the increase of descent rate, peaking at about  $v_d/v_h = 1.7$  due to the formation of the vortex ring. As for the aeroacoustics, a unique characteristic is the broadened noise spectra across the whole frequency range. Spectral humps at multiples of BPF occur, and the SPL values at BPF harmonics are increased, especially for the second BPF tone. The overall noise level generally exhibits an increasing trend with the descent rates until  $v_d$  reaches a relatively high value of 10 m/s. Then the nearfield flow structures and the corresponding surface noise sources from the numerical simulation results are presented and discussed. The opposing freestream directs the convecting trajectory of the tip vortices radially, progressively forming large recirculation regions around the blade tips as the descent rate increases. The rotor wake is expanded and finally shifted above the rotor at high descent rates. A high level of turbulent kinetic energy near the blade tips, especially under the VRS, is observed, which indicates strong interactions between the rotor and the turbulent vortices. The findings from the numerical acoustic prediction are similar to the experiments, which justifies the reliability of the current numerical model. Haystacking-like spectral humps are produced at multiples of BPF, and the additional noise mainly radiates in the upstream and downstream directions. From the on-surface noise source map, it is deduced that the principle noise generation mechanism in descending flight is the blade successively cutting through the same turbulent structures in its own wake, producing strong pressure fluctuations at the leading edge and radiating distinctive unsteady loading noise.

## ACKNOWLEDGMENTS

This work is supported by the National Key R&D Program of China (2018YFE0183800) and Hong Kong Research Grant Council (RGC 16202520 and 16206422). The authors would like to thank National Supercomputing Center in Guangzhou Nansha Sub-center and HKUST Fok Ying Tung Research Institute for providing high-performance computational resources.

## APPENDIX A: INSTALLATION EFFECT OF THE SUPPORTING TOWER

In Sec. IV, the influence of the wind tunnel outlet and the flow collector is discussed, which shows the non-negligible influence on the far-field noise. Here the effect of the installation method of the test rig will be investigated. Figure 23 shows the two configurations considered in this work, with the supporting tower placed downstream and upstream of the rotor. Although the tower is designed to be far away from the rotor (more than twice the rotor radius), there might still be some influence on the aerodynamic and aeroacoustic performance.

Figure 24(a) presents the rotor hovering performance at various rotational speeds. When the tower is placed upstream, the measured mean thrust is about 10% less than placed downstream. One possible reason is that the upstream cylinder-shaped tower causes a velocity deficit and leads to thrust loss. The results from our previous measurement in anechoic chamber [25], which also

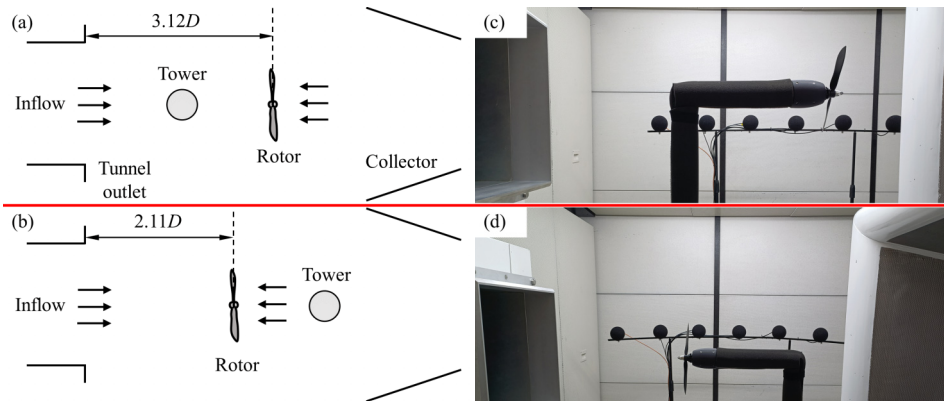


FIG. 23. Schematics and of two different test rig configurations: (a) tower placed downstream and (b) tower placed upstream. Photos of the setup: (c) tower placed downstream and (d) tower placed upstream.

adopts the downstream tower configuration, are compared with the measured results in this work to exclude the flow recirculation effect. No significant change is found between the two results, which suggests that the tower location is the critical factor of the mean thrust. In contrast, the torque results show less discrepancy between the three configurations. Figures 24(b) and 24(c) compare the thrust and torque of the rotor at 90 RPS and different descent rates. It is found that both the thrust and the torque are reduced to different extents.

Figures 25(a) and 25(b) compare the noise spectra at both in-plane and out-of-plane observers for the rotor in hover, respectively. The noise level of the first BPF tone for the upstream tower configuration is slightly lower than the downstream tower configuration, which is related to the steady loading noise caused by the thrust loss. Besides, the noise spectra show no significant difference except for the second and third BPF tones at  $\theta = 120^\circ$ , where the upstream tower configuration shows higher BPF tonal peaks. The corresponding mechanism is probably the passage of the blades through tower wakes, resulting in additional unsteady loading noise, which occurs at BPF-related frequencies. Moreover, Figure 25(c) and 25(d) compare the corresponding noise spectra at  $v_d = 10$  m/s. Interestingly, for the downstream tower, the spectral humps at the second BPF show a higher peak value at the in-plane observer but a lower peak value at the out-of-plane observer. One

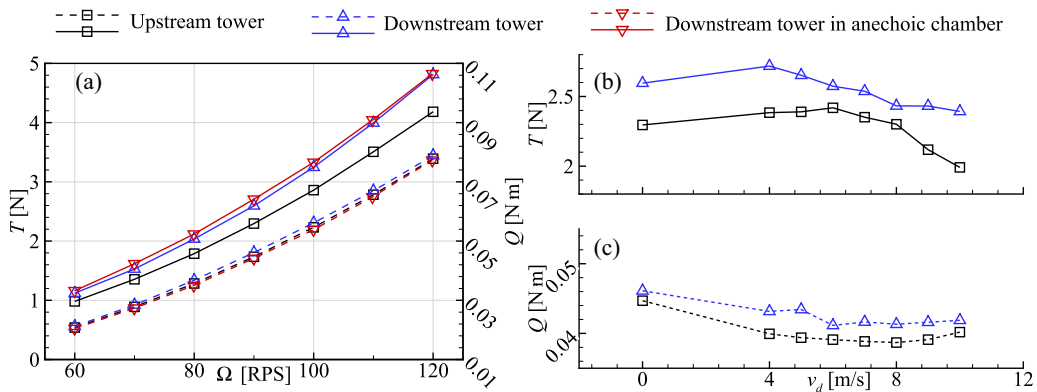


FIG. 24. (a) Thrust and torque measurements for hovering rotor operating at different rotational speeds. (b) Thrust and (c) torque comparison between two test rig configurations with different tower locations for rotor operating at 90 RPS and different descent rates.

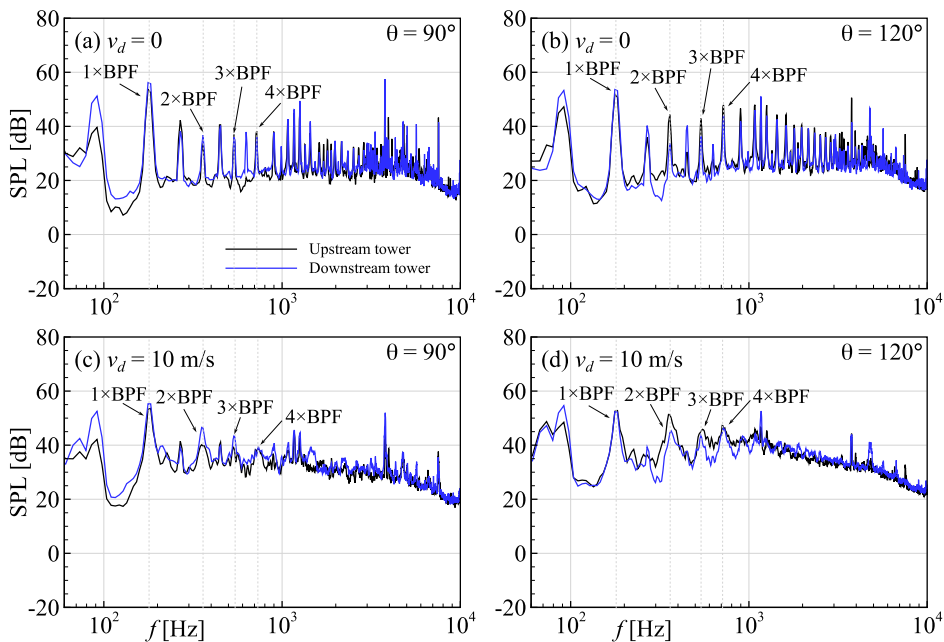


FIG. 25. Comparison of the noise spectra between two test rig configurations with different tower locations. The rotor is operating at 90 RPS.

explanation is that at high descent rates, the wake flow is reversed, making the downstream tower upstream of the rotor and changing the flow structures in the rotor wake. Nevertheless, although the installation has a non-negligible influence on the absolute thrust and noise results, the unique features (the broadened spectra and the BPF humps) in the descending flight and the relative trend with the descent rate remain the same. Therefore, this does not affect the main findings of this work.

## APPENDIX B: GRID CONVERGENCE STUDY OF NUMERICAL SIMULATIONS

Three grids with different cell numbers referred to as the coarse, the medium and the fine mesh, are examined respectively. The considered working condition of the rotor is hovering at 90 RPS. Table II shows the cell numbers and the corresponding aerodynamic mean force results for the three grids. An encouraging convergence for both thrust and torque is obtained.

Figure 26(a) presents the noise spectra at  $\theta = 90^\circ$  for the three grids. The coarse mesh seems to underpredict the broadband noise at  $f > 8000$  Hz, whereas the medium and the fine mesh show similar results. The fine mesh exhibits a slightly lower level of scattering than the medium mesh. Figure 26(b) shows the OASPL directivity for  $60 \text{ Hz} \leq f \leq 10000 \text{ Hz}$ . The overall disparity between the three grids is within 2 dB. In this work, the results from the fine mesh are used.

TABLE II. Cell number, time-averaged thrust, and torque for different grids.

Case	Cell number (millions)	$\bar{T}$ (N)	$\bar{Q}$ (N m)
Coarse	8.35	2.59	0.045
Medium	13.7	2.66	0.045
Fine	20.3	2.65	0.045



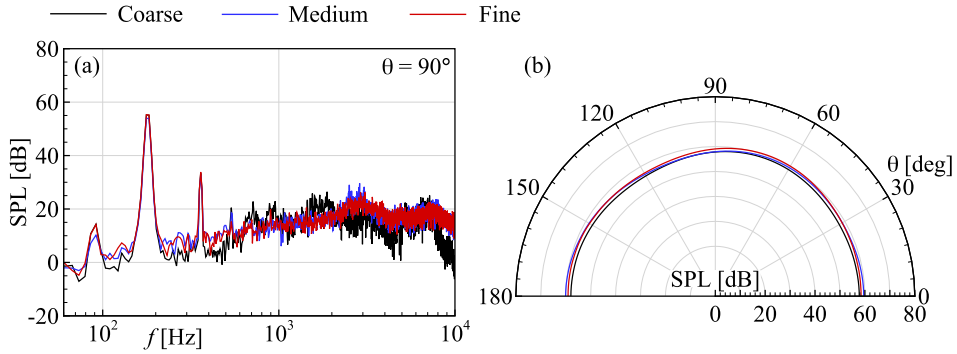


FIG. 26. Comparison of (a) the noise spectra at  $\theta = 90^\circ$  and (b) the OASPL directivity across the whole frequency range of 60 to 10 000 Hz between the three grids. The rotor is operating at 90 RPS.

### APPENDIX C: DISCUSSIONS ON THE SHAFT-ORDER TONES IN EXPERIMENTS

By examining the results in Figs. 16(a) and 16(b), it is noted that there are multiple tones at the blade shaft frequency ( $0.5 \times \text{BPF}$ ) and its harmonics ( $1.5 \times \text{BPF}$ ,  $2.5 \times \text{BPF}$ ), which only exist in experiments but are not seen in simulations. Zawodny *et al.* [54] attributed these shaft-order tones to the blade-to-blade geometry difference. Recently, a study by Zhong *et al.* [18] suggested that the aerodynamic asymmetry caused by the rotor mass imbalance can cause tonal noise at the harmonics of the shaft frequency. Also, the geometrical imperfection could cause blade vibration and induce extra shaft-order tonal noise [19]. Since the cause of the experimental shaft-order tones is unclear, it is worth investigating the evolving trends in that these tones vary with the operating conditions. This section presents the experimental results of the shaft-order tones at different descent rates and rotational speeds.

Figure 27 shows the directivity of the first three shaft-order tones from  $v_d = 0$  to 10 m/s. The rotational speed of the rotor is 90 RPS for all cases. The noise at  $0.5 \times \text{BPF}$  shows a strong radiation pattern towards the upstream and downstream directions with a minimum SPL value at  $\theta = 80^\circ$ . When  $v_d$  is increased from 0 to 4 m/s, an overall increase of about 2 dB is observed. However, the further increase of  $v_d$  brings only small changes, which are in the range of the error bars. At  $1.5 \times \text{BPF}$ , the radiation in the rotation plane ( $\theta = 90^\circ$ ) is more substantial than both upstream and downstream directions. The variations of SPL values with the descent rate are minimal for all observer angles. At  $2.5 \times \text{BPF}$ , the noise production is more significant in the upstream than in the downstream directions. When  $v_d$  is increased, no distinct change exists except for  $\theta = 110^\circ$  and

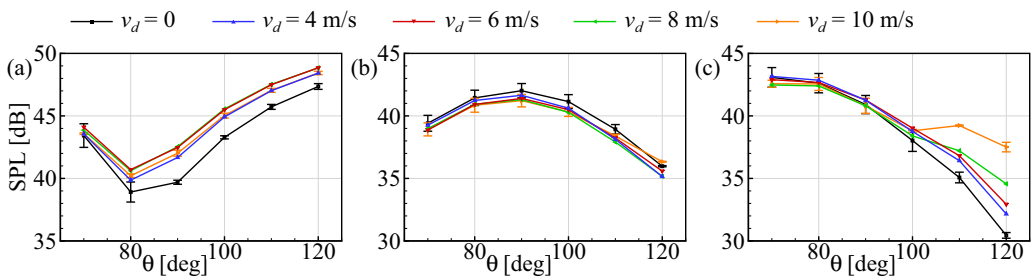


FIG. 27. Comparison of sound pressure level at various descent rates for different observer angles (a) at  $0.5 \times \text{BPF}$ , (b)  $1.5 \times \text{BPF}$ , and (c)  $2.5 \times \text{BPF}$ . The error bars indicate the uncertainty from repetitive measurements at the 95% confidence interval. Only the error bars of  $v_d = 0$  and 10 m/s are shown for clarity. The rotor is operating at 90 RPS.

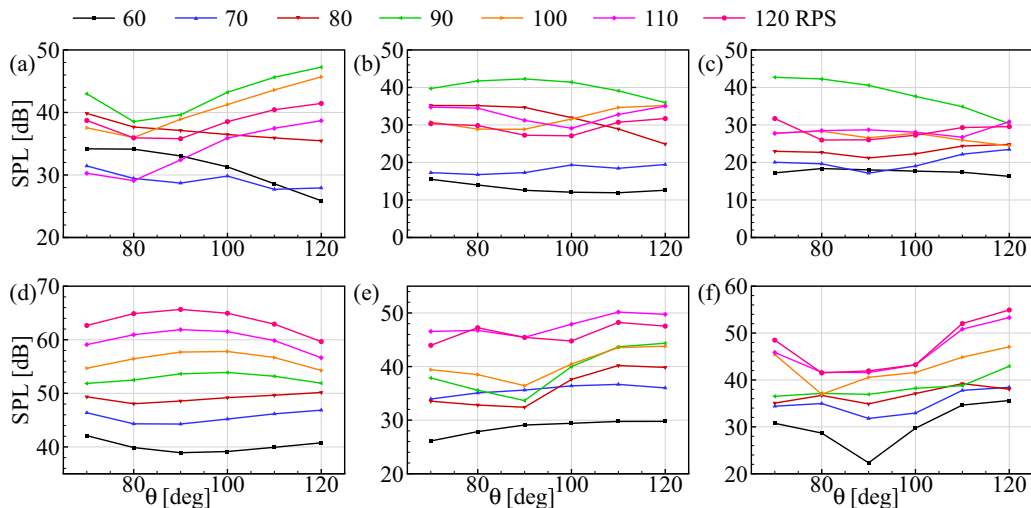


FIG. 28. Comparison of sound pressure level at various rotational speeds for different observer angles (a) at  $0.5 \times \text{BPF}$ , (b)  $1.5 \times \text{BPF}$ , (c)  $2.5 \times \text{BPF}$ , (d) at  $1 \times \text{BPF}$ , (e)  $2 \times \text{BPF}$ , and (f)  $3 \times \text{BPF}$ . The rotor is under hovering conditions.

$120^\circ$ , where higher descent rates lead to higher SPL values. Overall, the tonal noise at shaft-order frequencies is not sensitive to the rotor descent rate, and the directivity of each tone is hardly affected by the axial flows.

Figure 28 presents the variations of the SPL values on different rotational speeds. For the shaft-order tones shown in Figs. 28(a)–28(c), although the directivities for different rotational speeds vary and do not share a common pattern, a general trend can still be seen. With the rotational speed increase, the SPL values first increase, reaching a maximum at 90 RPS, and then decrease. This trend applies to all shaft-order tones at  $0.5 \times \text{BPF}$ ,  $1.5 \times \text{BPF}$ , and  $2.5 \times \text{BPF}$ , although the variation is not monotonous in some observer angles. The evolving trend of the tones at BPF harmonics is also shown in Figs. 28(d)–28(e) for comparison. The noise level shows a monotonically increasing trend with the descent rate, especially at the first BPF. The different characteristics between the tones at shaft-order frequencies and the BPF harmonics indicate that the shaft-order tones are less correlated to aerodynamic changes. Combined with previous findings that the shaft-order noise is insensitive to the descent rate, it is deduced that the shaft-order tones may be caused by the mechanical vibration of the rotor test system, which has the strongest excitation response at about 90 Hz.

- 
- [1] D. Floreano and R. J. Wood, Science, technology and the future of small autonomous drones, *Nature* **521**, 460 (2015).
  - [2] S. Rajendran and S. Srinivas, Air taxi service for urban mobility: A critical review of recent developments, future challenges, and opportunities, *Transport. Res. Part E: Logist. Transport. Rev.* **143**, 102090 (2020).
  - [3] A. Straubinger, R. Rothfeld, M. Shamiyeh, K. D. Büchter, J. Kaiser, and K. O. Plötner, An overview of current research and developments in urban air mobility—Setting the scene for UAM introduction, *J. Air Transp. Manage.* **87**, 101852 (2020).
  - [4] S. A. Rizzi, D. L. Huff, D. D. Boyd, P. Bent, R. Boeing, S. Louis, B. S. Henderson, R. Snider, B. Flight, and F. Worth, Urban air mobility noise: Current practice, gaps, and recommendations, NASA/TP-2020-5007433 (2020), <https://ntrs.nasa.gov/citations/20205007433>.
  - [5] S. Zhong, P. Zhou, R. Fattah, and X. Zhang, A revisit of the tonal noise of small rotors, *Proc. R. Soc. A* **476**, 20200491 (2020).

- [6] J. Wu, H. Jiang, Z. Ma, W. Chen, and X. Huang, Numerical investigation of airfoil-rotor interaction at low Reynolds number, *Phys. Fluids* **34**, 025118 (2022).
- [7] G. Romani, E. Grande, F. Avallone, D. Ragni, and D. Casalino, Computational study of flow incidence effects on the aeroacoustics of low blade-tip Mach number propellers, *Aerosp. Sci. Technol.* **120**, 107275 (2022).
- [8] R. R. Mankbadi, S. O. Afari, and V. V. Golubev, High-fidelity simulations of noise generation in a propeller-driven unmanned aerial vehicle, *AIAA J.* **59**, 1020 (2021).
- [9] R. Gojon, T. Jardin, and H. Parisot-Dupuis, Experimental investigation of low Reynolds number rotor noise, *J. Acoust. Soc. Am.* **149**, 3813 (2021).
- [10] H. Hu, Y. Yang, Y. Liu, X. Liu, and Y. Wang, Aerodynamic and aeroacoustic investigations of multi-copter rotors with leading edge serrations during forward flight, *Aerosp. Sci. Technol.* **112**, 106669 (2021).
- [11] H. Jiang, H. Wu, W. Chen, P. Zhou, S. Zhong, X. Zhang, G. Zhou, and B. Chen, Toward high-efficiency low-noise propellers: A numerical and experimental study, *Phys. Fluids* **34**, 076116 (2022).
- [12] S. Glegg and W. Devenport, *Aeroacoustics of Low Mach Number Flows Fundamentals, Analysis, and Measurement* (Academic Press, San Diego, CA, 2017), pp. 3–8.
- [13] Gutin, On the sound field of a rotating propeller, NACA-TM-1995 (1948), <https://ntrs.nasa.gov/citations/20030068996>.
- [14] C. Morfey, Rotating blades and aerodynamic sound, *J. Sound Vib.* **28**, 587 (1973).
- [15] D. B. Hanson, Near-field frequency-domain theory for propeller noise, *AIAA J.* **23**, 499 (1985).
- [16] Y. H. Yu, Rotor blade-vortex interaction noise, *Prog. Aerosp. Sci.* **36**, 97 (2000).
- [17] Y. Wu, M. J. Kingan, and S. T. Go, Propeller-strut interaction tone noise, *Phys. Fluids* **34**, 055116 (2022).
- [18] S. Zhong, P. Zhou, W. Chen, H. Jiang, H. Wu, and X. Zhang, An investigation of rotor aeroacoustics with unsteady motions and uncertainty factors, *J. Fluid Mech.* **956**, A16 (2023).
- [19] Y. Li, H. Wu, H. Jiang, S. Zhong, and X. Zhang, Computational aeroacoustics study of propellers with vibrational motion, *AIAA J.* **61**, 3091 (2023).
- [20] R. K. Amiet, Noise produced by turbulent flow into a propeller or helicopter rotor, *AIAA J.* **15**, 307 (1977).
- [21] R. H. Schlinker and R. K. Amiet, Helicopter rotor trailing edge noise, NASA-CR-3470 (1981), <https://doi.org/10.2514/6.1981-2001>.
- [22] T. Brooks, D. Pope, and M. Marcolini, Airfoil self-noise and prediction, NASA-RP-1218 (1989), <https://ntrs.nasa.gov/citations/19890016302>.
- [23] Y. Yang, Y. Liu, Y. Li, E. Arcondoulis, and Y. Wang, Aerodynamic and aeroacoustic performance of an isolated multicopter rotor during forward flight, *AIAA J.* **58**, 1171 (2020).
- [24] Y. Yauwenas, J. Fischer, D. Moreau, and C. Doolan, The effect of inflow disturbance on drone propeller noise, in *25th AIAA/CEAS Aeroacoustics Conference*, AIAA Paper 2019-2633 (2019), <https://doi.org/10.2514/6.2019-2663>.
- [25] H. Wu, W. Chen, H. Jiang, S. Zhong, and X. Zhang, Experimental investigation of the effect of sectional airfoil profile deviation on propeller noise, *Phys. Fluids* **35**, 027104 (2023).
- [26] D. Casalino, E. Grande, G. Romani, D. Ragni, and F. Avallone, Definition of a benchmark for low Reynolds number propeller aeroacoustics, *Aerosp. Sci. Technol.* **113**, 106707 (2021).
- [27] C. Nardari, D. Casalino, F. Polidoro, V. Coralic, P.-T. Lew, and J. Brodie, Numerical and experimental investigation of flow confinement effects on UAV rotor noise, AIAA Paper 2019-2497 (2019), <https://doi.org/10.2514/6.2019-2497>.
- [28] H. Lee and D. J. Lee, Rotor interactional effects on aerodynamic and noise characteristics of a small multicopter unmanned aerial vehicle, *Phys. Fluids* **32**, 047107 (2020).
- [29] N. S. Zawodny and D. D. Boyd, Investigation of rotor-airframe interaction noise associated with small-scale rotary-wing unmanned aircraft systems, *J. Am. Helicopter Soc.* **65**, 1 (2020).
- [30] J. Stack, F. X. Caradonna, and Ö. Savaş, Flow visualizations and extended thrust time histories of rotor vortex wakes in descent, *J. Am. Helicopt. Soc.* **50**, 279 (2005).
- [31] J. Seddon and S. Newman, *Basic Helicopter Aerodynamics* (John Wiley & Sons, New York, 2011), Chap. 2, pp. 23–61.

- [32] A. Brand, M. Dreier, R. Kisor, and T. Wood, The nature of vortex ring state, *J. Am. Helicopt. Soc.* **56**, 22001 (2011).
- [33] J. G. Leishman, M. J. Bhagwat, and S. Ananthan, The vortex ring state as a spatially and temporally developing wake instability, *J. Am. Helicopt. Soc.* **49**, 160 (2004).
- [34] O. Shetty and M. Selig, Small-scale propellers operating in the vortex ring state, in *49th AIAA Aerospace Sciences Meeting including the New Horizons Forum and Aerospace Exposition*, AIAA Paper 2011-1254 (2011), <https://doi.org/10.2514/6.2011-1254>.
- [35] M. P. Kinzel, J. K. Cornelius, S. Schmitz, J. L. Palacios, J. W. Langelaan, D. Adams, and R. Lorenz, An investigation of the behavior of a coaxial rotor in descent and ground effect, in *AIAA Scitech 2019 Forum*, AIAA Paper 2019-1098 (2019), <https://doi.org/10.2514/6.2019-1098>.
- [36] G. Throneberry, A. Takeshita, C. M. Hocut, F. Shu, and A. Abdelkefi, Multi-rotor wake characterization and visualization in ascending and descending flight, *Exp. Fluids* **63**, 98 (2022).
- [37] S. Chae, S. Lee, and J. Kim, Effects of rotor-rotor interaction on the wake characteristics of twin rotors in axial descent, *J. Fluid Mech.* **952**, A31 (2022).
- [38] M. Veismann, Effects of rotor separation on the axial descent performance of dual-rotor configurations, *Flow* **3**, E7 (2023).
- [39] M. Veismann, D. Yos, and M. Gharib, Parametric study of small-scale rotors in axial descent, *Phys. Fluids* **34**, 035124 (2022).
- [40] P. Spalart, S. Deck, M. Shur, K. Squires, M. Strelets, and A. Travin, A new version of detached-eddy simulation, resistant to ambiguous grid densities, *Theor. Comput. Fluid Dyn.* **20**, 181 (2006).
- [41] W. Yi, P. Zhou, Y. Fang, J. Guo, S. Zhong, X. Zhang, X. Huang, G. Zhou, and B. Chen, Design and characterization of a multifunctional low-speed anechoic wind tunnel at HKUST, *Aerosp. Sci. Technol.* **115**, 106814 (2021).
- [42] H. Jiang and X. Zhang, An acoustic-wave preserved artificial compressibility method for low-Mach-number aeroacoustic simulations, *J. Sound Vib.* **516**, 116505 (2022).
- [43] P. Spalart and S. Allmaras, A one-equation turbulence model for aerodynamic flows, in *30th Aerospace Sciences Meeting and Exhibit*, AIAA Paper 1992-439 (1992), <https://doi.org/10.2514/6.1992-439>.
- [44] J. E. Ffowcs-Williams and D. L. Hawkings, Sound generation by turbulence and surfaces in arbitrary motion, *Philos. Trans. R. Soc. Lond. Ser. A* **264**, 321 (1969).
- [45] F. Farassat, Derivation of formulations 1 and 1A of Farassat, NASA/TM-2007-214853 (2007), <https://ntrs.nasa.gov/citations/20070010579>.
- [46] P. Welch, The use of fast Fourier transform for the estimation of power spectra: A method based on time averaging over short, modified periodograms, *IEEE Trans. Audio Electroacoust.* **15**, 70 (1967).
- [47] R. Hogg, J. McKean, and A. Craig, *Introduction to Mathematical Statistics* (Pearson Education, Boston, 2005).
- [48] G. T. Chapman, Topological classification of flow separation on three-dimensional bodies, in *24th Aerospace Sciences Meeting*, AIAA Paper 1986-0485 (1986), <https://doi.org/10.2514/6.1986-485>.
- [49] J. H. Stephenson, D. Weitsman, and N. S. Zawodny, Effects of flow recirculation on unmanned aircraft system (UAS) acoustic measurements in closed anechoic chambers, *J. Acoust. Soc. Am.* **145**, 1153 (2019).
- [50] H. H. Murray, W. J. Devenport, W. N. Alexander, S. A. L. Glegg, and D. Wisda, Aeroacoustics of a rotor ingesting a planar boundary layer at high thrust, *J. Fluid Mech.* **850**, 212 (2018).
- [51] S. H. Wasala, R. C. Storey, S. E. Norris, and J. E. Cater, Aeroacoustic noise prediction for wind turbines using large eddy simulation, *J. Wind Eng. Ind. Aerodynam.* **145**, 17 (2015).
- [52] X. Tan, Z. Yang, X. Tan, X. Wu, and J. Zhang, Vortex structures and aeroacoustic performance of the flow field of the pantograph, *J. Sound Vib.* **432**, 17 (2018).
- [53] J. Yangzhou, J. Wu, Z. Ma, and X. Huang, Aeroacoustic sources analysis of wake-ingesting propeller noise, *J. Fluid Mech.* **962**, A29 (2023).
- [54] N. S. Zawodny, D. B. Jr., and C. L. Burley, Acoustic characterization and prediction of representative, small-scale rotary-wing unmanned aircraft system components, NASA TR NF1676L-22587 (2016), <https://ntrs.nasa.gov/citations/20160009054>.